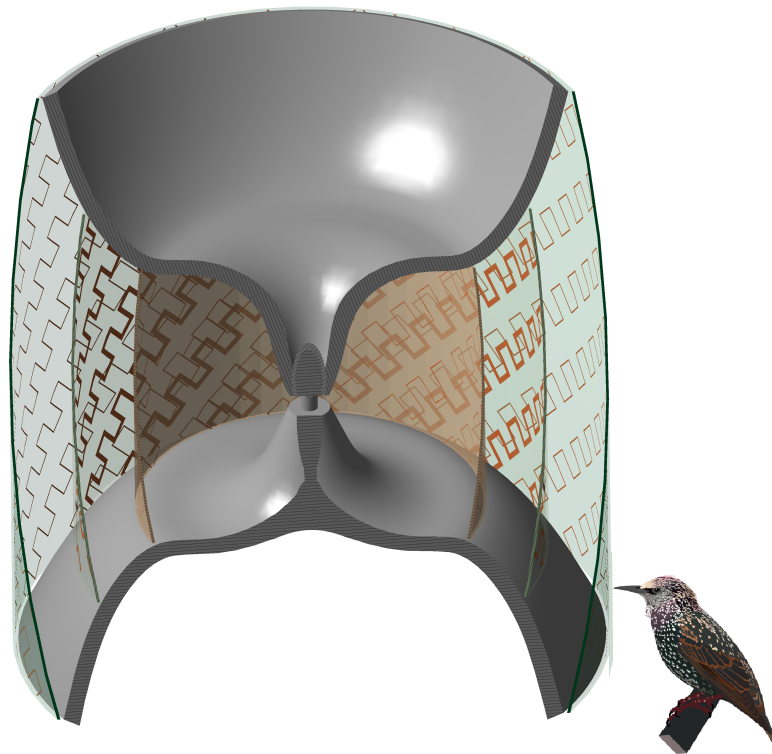




**CHALMERS**  
UNIVERSITY OF TECHNOLOGY

---



# **A New Circularly Polarized Biconical Horn for Spacecraft TT&C**

Master's thesis in Electrical Engineering

**SIMON OLVHAMMAR**

---

Department of Electrical Engineering  
CHALMERS UNIVERSITY OF TECHNOLOGY  
Gothenburg, Sweden 2018



*Somewhere, something incredible is waiting to be known.*

*Carl Sagan*



MASTER'S THESIS

**A New Circularly Polarized Biconical Horn for  
Spacecraft TT&C**

SIMON OLVHAMMAR



**CHALMERS**  
UNIVERSITY OF TECHNOLOGY

Department of Electrical Engineering  
CHALMERS UNIVERSITY OF TECHNOLOGY  
Gothenburg, Sweden 2018

A New Circularly Polarized Biconical Horn  
for Spacecraft TT&C  
SIMON OLVHAMMAR

© SIMON OLVHAMMAR, 2018.

E-mail: [simn@chalmers.se](mailto:simn@chalmers.se);  
Phone: +46 (0)73 0432 972

Supervisor: Dr. Johan Wettergren, RUAG Space AB  
Examiner: Prof. Jian Yang, Department of Electrical Engineering, Chalmers University of Technology

Master's Thesis  
Department of Electrical Engineering  
Chalmers University of Technology  
SE-412 96 Gothenburg  
Telephone +46 (0)31 772 1000

RUAG Space AB  
SE-412 76 Gothenburg  
Telephone +46 (0)31 735 0000

Cover: The proposed biconical horn antenna consisting of a stochastically optimized spline-profile and a three layer polarizer designed with a robust flame resistant fibreglass substrate.

Typeset in L<sup>A</sup>T<sub>E</sub>X  
Gothenburg, Sweden 2018

A New Circularly Polarized Biconical Horn  
for Spacecraft TT&C  
Simon Olvhammar  
Department of Electrical Engineering  
Chalmers University of Technology

## Abstract

In the early days of space exploration simple monopole antennas were used in state-of-art spacecraft systems. Time changes and so does the requirements and new compact, cost effective and high performing antenna systems need to be developed. Many of the current omnidirectional antennas for space are complex, hard to manufacture and thus very expensive. In this thesis we will study a mechanically simple coaxially fed biconical antenna and evolve the design using 21th century methods that has not been applied to the topology before. We propose a Right Handed Circular Polarized (RHCP) Toroidal Low Gain Antenna (TLGA) that can be used for dual band Telemetry, Tracking and Command (TT&C) in spacecraft and satellite systems. The antenna is designed for single element operation whereas most current space TLGAs require two elements, one for the receiving chain (RX) and one for the transmitting (TX).

The commonly used profile for the biconical antenna is the straight. In this thesis, we investigate a set of other profiles, which are used in the design of horn antennas, but for the bicone antenna which at a fundamental level is a broadband dipole. We also propose to use a new method for beam shaping and side lobe reduction by employing a smooth profile that is spline-defined and stochastically optimized. This represent a new development of the bicone antenna but the method has been successfully applied to e.g. state-of-the-art horn antennas in the Square Kilometer Array (SKA) project. Furthermore, a three layer meander type polarizer is designed, using a very robust flame resistant fibreglass substrate (FR4). The polarizer will be cleverly integrated in the profile of the antenna to provide the required mechanical stiffness for a spacecraft launch. The electrical design of the antenna is also prepared for the harsh environment of space where e.g. thermal mismatches can be accounted for by using a capacitively coupled coaxial excitation. The design also allows for an outer layer of e.g. germanium Kapton to protect against radiation charging.

Birds, such as starlings, and other biological creatures exhibiting swarm behaviour deserve immense credit for their contribution to science. The proposed antennas have achieved radiation patterns, and other characteristics, that never would have been possible without biologically inspired optimization algorithms. As such, the starling bird has earned a place on the front page of this report next to the presented TLGA which it has optimized.

Keywords: space, antenna, satellite, biconical horn, telemetry, tracking and command, circular polarisation, stochastic optimization, meander-polarizer.



## Acknowledgements

First of all, I would like to express my gratitude to Dr. Johan Wettergren at RUAG Space who provided me with the opportunity to carry out this thesis. Dr. Wettergren has also been my main supervisor during the project and he has supported me at all times. Furthermore, I would also like to thank everybody at the department of Antenna Electrical Design at RUAG Space. Especially, I would like to thank Dr. Joakim Johansson, Jan Zackrisson, Susanne Schilliger Kildal, Mikael Öhgren, Erik Geterud and Per Magnusson for providing me with knowledge and insights on design, modelling and optimization techniques. I also want to reach out to the people at ANSYS for granting me a license which provided me the means to simulate my designs and ideas.

I was first introduced to the idea of using the biological behaviours of e.g. a particle swarm to optimize antennas at Onsala Space Observatory, where I have worked part time during my studies. The observatory is also a place where I have gained knowledge in other areas, apart from antennas, such as software development which has been very helpful in my work. I would like to thank Prof. Gunnar Elgered who was the person that introduced me to observatory and initiated my first project. Throughout this time Dr. Peter Forkman has been very supportive and has always believed in my work. Furthermore, I would like to thank Dr. Miroslav Pantaleev and Jonas Flygare for introducing me to the Quad Ridge Flared Horn which will be used in several bands for the Square Kilometer Array (SKA) project. I learned a great deal from them regarding the design and optimization of state-of-the-art antennas.

Simon Olvhammar, Gothenburg, June 2018



# Contents

|  |             |
|--|-------------|
| <b>List of Figures</b>   | <b>xiii</b> |
| <b>List of Tables</b>  | <b>xvii</b> |
| <b>1 Introduction and Background</b>                             | <b>1</b>    |
| 1.1 Telemetry, Tracking and Command Spacecraft Systems . . . . . | 2           |
| 1.1.1 TT&C Back-ends . . . . .                                   | 3           |
| 1.1.2 Antenna Configurations . . . . .                           | 4           |
| 1.2 Toroidal Coverage Antennas . . . . .                         | 5           |
| 1.3 Thesis Organization and Scope . . . . .                      | 7           |
| <b>2 Biconical Horn Antennas</b>                                 | <b>9</b>    |
| 2.1 Mode Content and Directivity Design Curves . . . . .         | 9           |
| 2.2 Azimuth and Elevation Patterns . . . . .                     | 12          |
| 2.3 Input Impedance . . . . .                                    | 14          |
| 2.4 Profile Options . . . . .                                    | 15          |
| 2.5 Corrugations . . . . .                                       | 17          |
| <b>3 Meander-Line Polarizers</b>                                 | <b>19</b>   |
| 3.1 Design Theory . . . . .                                      | 19          |
| 3.2 Plane to Cylinder Conversion . . . . .                       | 20          |
| <b>4 Specifications and Requirements</b>                         | <b>23</b>   |
| 4.1 Electromagnetic . . . . .                                    | 23          |
| 4.1.1 Frequency and Bandwidth . . . . .                          | 23          |
| 4.1.2 Gain . . . . .   | 23          |
| 4.1.3 Return Loss . . . . .                                      | 24          |
| 4.1.4 Azimuth Ripple . . . . .                                   | 24          |
| 4.1.5 Polarisation . . . . .                                     | 24          |
| 4.1.6 Axial Ratio . . . . .                                      | 24          |
| 4.1.7 Cross-Polar Discrimination . . . . .                       | 25          |
| 4.1.8 Side-lobes . . . . .                                       | 25          |
| 4.2 Mechanical . . . . .   | 25          |
| 4.2.1 Margin of Safety and Stiffness . . . . .                   | 26          |
| 4.2.2 Sinusoidal Stationary Vibration . . . . .                  | 27          |
| 4.2.3 Random Response Analysis . . . . .                         | 27          |
| 4.2.4 Non-stationary Vibration . . . . .                         | 28          |

|          |  |           |
|----------|--|-----------|
| 4.3      | The Space Environment . . . . .                  | 28        |
| 4.3.1    | Multipaction . . . . .                           | 28        |
| 4.3.2    | Outgassing . . . . .                             | 29        |
| 4.3.3    | Thermal Analysis . . . . .                       | 29        |
| <b>5</b> | <b>Design Methods</b>                            | <b>31</b> |
| 5.1      | Electromagnetic Modelling . . . . .              | 31        |
| 5.2      | Optimization . . . . .                           | 31        |
| 5.2.1    | Biologically Inspired Algorithms . . . . .       | 32        |
| 5.2.2    | Fitness Evaluation . . . . .                     | 32        |
| 5.2.3    | Spline-defined profile . . . . .                 | 34        |
| 5.2.4    | Optimization System Routine . . . . .            | 36        |
| 5.3      | Mechanical Design . . . . .                      | 37        |
| <b>6</b> | <b>Results</b>                                   | <b>41</b> |
| 6.1      | Selection of Biconical Horn Profile . . . . .    | 41        |
| 6.1.1    | Directivity Design Curves . . . . .              | 41        |
| 6.1.2    | Beam Patterns of Analytical Profiles . . . . .   | 42        |
| 6.2      | Dual Band Vertically Polarized TLGA . . . . .    | 46        |
| 6.2.1    | Spline-defined Profile Optimization . . . . .    | 46        |
| 6.2.2    | Elevation Beam Pattern . . . . .                 | 48        |
| 6.2.3    | Return Loss . . . . .                            | 49        |
| 6.2.4    | Summary and Specifications, V-pol TLGA . . . . . | 49        |
| 6.3      | Three Layer Meander-Line Polarizer . . . . .     | 50        |
| 6.3.1    | Plane Meander Array . . . . .                    | 50        |
| 6.3.2    | Ideal AR, XPD and Return Loss . . . . .          | 51        |
| 6.3.3    | Cylindrical Wrapping of Polarizer . . . . .      | 53        |
| 6.4      | Dual Band Circularly Polarized TLGA . . . . .    | 55        |
| 6.4.1    | Positioning of Polarizer Layers . . . . .        | 55        |
| 6.4.2    | Elevation Beam Patterns . . . . .                | 55        |
| 6.4.3    | Axial Ratio and XPD . . . . .                    | 56        |
| 6.4.4    | Reflection Coefficients . . . . .                | 59        |
| 6.4.5    | Summary and Specifications, RHCP TLGA . . . . .  | 60        |
| 6.5      | RHCP TLGA as Single Band Antenna . . . . .       | 62        |
| <b>7</b> | <b>Discussion and Conclusions</b>                | <b>65</b> |
| 7.1      | Future work . . . . .                            | 65        |
| 7.1.1    | XPD and Return Loss Improvements . . . . .       | 66        |
| 7.1.2    | Mechanical and Thermal Design . . . . .          | 66        |
|          | <b>Bibliography</b>                              | <b>69</b> |

# List of Figures

|     |  |    |
|-----|--|----|
| 1.1 | Simplified system architecture for satellite TT&C communication. The upper and lower diagram display the receiving and transmitting chain respectively. . . . .  | 3  |
| 1.2 | Illustration of the most common TT&C antenna system used by North American satellite suppliers. Two Wide Coverage Antennas (WCAs) are used in combination with a Toroidal Low Gain Antenna (TLGA) to provide full coverage around the satellite. . . . .                                     | 4  |
| 1.3 | Illustration of a toroidal shaped beam pattern as radiated from e.g. a biconical horn antenna positioned vertically in the center of the toroid. . . . .   | 6  |
| 1.4 | A Toroidal Low Gain Antenna (TLGA) developed by RUAG Space AB for $K_u$ -Band. The main antenna elements are two bicones, fed by an array of slots using cylindrical waveguides and septum polarizers. The upper (smaller) bicone is the RX antenna element and the lower is the TX. . . . . | 7  |
| 2.1 | Geometry for a straight profile biconical horn. H denotes the aperture height, R the cone radius or antenna radius, D is the diameter of the gap and G the gap size. . . . .   | 11 |
| 2.2 | Theoretical directivity as a function of the aperture height for a straight profile biconical horn. For each directivity curve the cone radius is constant and linearly increasing from one free space wavelength ( $\lambda_0$ ) to five. . . . .   | 13 |
| 2.3 | Directivity contour plots for a straight profile biconical horn. The contour plot can be useful to find optimal antenna geometries, in terms of the cone radius and aperture height. Furthermore, it can provide information on the gain variation over a specified bandwidth. . . . .       | 13 |
| 2.4 | Relative E plane pattern of a sectoral horn for different aperture phase error (S). The E plane pattern of a sectoral horn corresponds, in good approximation, to the E plane pattern of a biconical horn. . . . .   | 14 |
| 2.5 | Input impedance, reactance in blue and resistance in red, of a biconical horn antenna for a constant cone angle of 50 degrees. The characteristic impedance ( $Z_0$ ) of the antenna is displayed in black. . . . .  | 16 |
| 2.6 | Actual, simulated, input resistances for TEM excited biconical horns of different antenna radii and gap sizes. The black, dotted, line displays the theoretical characteristic resistance as defined by equation 2.8. . . . .  | 18 |

|     |  |    |
|-----|--|----|
| 2.7 | The profiles that will be investigated for the biconical horn. Two variants of the sinusoidal profile are considered, i.e. using two different orders (p) and linear tapers (A). . . . .   | 18 |
| 3.1 | Single sheet meander design illustration using a Smith Chart. . . . .  | 21 |
| 3.2 | Design parameters for a meander unit cell. I.e. the cell periodicity (p), the cell height (w) and width of the meander lines (d). . . . .  | 22 |
| 3.3 | Illustration of how the incident field should be aligned in relation meander plane for linear to circular polarisation conversion. The cell periodicity (p) and the distance between the meander lines (a) is also defined. . . . .  | 22 |
| 3.4 | Parameter illustration for a three layer meander line polarizer. I.e. the substrate thickness, t, and the spacing between the layers, s. The spacing between the layers should be around one quarter wavelength at the design frequency. . . . .   | 22 |
| 5.1 | Illustration of the fitness functions for the main beam and side-lobes. We require a gain greater than - 1 dBi for the main beam and lower than -5 dBi and -10 dBi respectively for the side lobe areas that are displayed in the figure. . . . .  | 34 |
| 5.2 | Illustration of a numerically defined profile for the biconical horn. The profile is defined by seven points, excluding the start value of the profile defining the gap size and diameter. Only symmetric bicones are considered and as such the points are mirrored and extruded in y . . . . .   | 35 |
| 5.3 | Block diagram of the optimization procedure using Matlab and VBA Scripting in combination with the EM-Modelling tool Ansys HFSS. . . . .   | 38 |
| 5.4 | Block diagram of a typical mechanical design procedure for a space antenna. The antenna simulation on a complete satellite is often left out and the antenna element characteristics are considered sufficient. . . . .  | 39 |
| 5.5 | Illustration of a deformed TEM excited biconical horn. The deformation or even total mechanical failure, i.e. that the center conductor is breached, will occur during the launch of the spacecraft if not properly stabilized by an external structure. For a ground based application the center conductor will not deform unless heavily stressed. . . . .  | 39 |
| 6.1 | Directivity as a function of aperture height for a number of different profiles. In the upper plot the bicone has a radius of one wavelength while in the lower plot the radius is two wavelengths. All results are simulated except the red curve in the upper plot which displays a theoretical case for a straight profile bicone antenna with a radius of one wavelength, refer to Figure 2.2 or 2.3. The results were retrieved by sweeping the antenna geometry using Matlab in combination with HFSS. . . . . | 43 |
| 6.2 | Geometric illustration of the profiles that were investigated. I.e. the linear, exponential, parabolic, tangential and two variants of the sinusoidal profile of different order (p) and linear taper (A). The corresponding elevation patterns are displayed in Figure 6.4. . . . .   | 44 |

|      |  |    |
|------|--|----|
| 6.3  | Comparison of directivity versus aperture height for the sinusoidal and the straight profile respectively. Note that the curve for sinusoidal profile is derived using a cone radius of one wavelength whereas the straight profile has a radius of two wavelengths. . . . .   | 44 |
| 6.4  | Radiation patterns for the studied profiles. The red curves indicate the pattern at the center of the TX band and black curve the center of the RX band i.e. 8475.0 and 7167.5 MHz respectively. The gain mask is indicated in dotted blue. . . . .  | 45 |
| 6.5  | Iteration fitness for an optimization run on the X-Band TLGA. The algorithm is focusing on the horn profile using a total of 14 geometry parameters. . . . .   | 46 |
| 6.6  | Geometry and profile illustration of the proposed vertically polarized biconical horn. The profile is derived using a stochastic algorithm applied on the spline points of the horn. . . . .   | 47 |
| 6.7  | Radiation pattern, in $\theta$ , for the vertically polarized spline-optimized biconical horn. The red curves display the lower, upper and center frequency of the TX band and equivalently for RX band in blue. The gain mask is indicated in dotted black. . . . .   | 48 |
| 6.8  | Simulated reflection coefficient for the vertically polarized TLGA. The return loss is greater than 18 dB for both the TX and RX band with a center frequency of 8475 and 7167.5 MHz respectively. . . . .   | 49 |
| 6.9  | Illustration of the meander unit cell modelling, one for each polarisation component as defined by the red arrows. The blue arrow is an indication that the measured characteristics are de-embedded. Symmetry planes are employed in order to simulate an infinite array of meander cells with an incident plane wave. . . . .  | 51 |
| 6.10 | Axial ratio, cross-polar discrimination and reflection coefficients, perpendicular and parallel components, for the meander line polarizer. The results assume plane wave incidence on three layers of infinite extension. . . . .   | 52 |
| 6.11 | The figure display the rhombic shaped meander plane that is wrapped around a cylinder, in this case a FR4-epoxy substrate. The meander plane is the result from an intersection between a very large quadratic shaped polarizer plane and a rhombic parallelogram. The geometry of the parallelogram is matched to the dimensions of the cylinder with radius R and height H. . . . .                            | 54 |
| 6.12 | Illustration of the three layer polarizer used for the biconical antenna. The meander lines are wrapped on a cylindrical FR4 substrate with a thickness of 12 mil. The innermost layer is the left cylinder and the outermost to the right. Note that the illustrated polarizers are scaled versions of the actual design. Refer to Figure 6.13 to observe how the layers are implemented in the design. . . . . | 54 |

|      |  |    |
|------|--|----|
| 6.13 | A cutting plane illustration of the circular polarized TLGA. The figure displays the relative positions of each polarizer layer. The spherical phase front, incident on the layers, is also illustrated. The blue area indicates the dielectric that should be used in the capacitive coupling of the coaxial feed. . . . .  | 56 |
| 6.14 | Beam patterns, with co and cross-polarisation in red and blue respectively, for the two bands i.e. RX band upper plot and TX lower plot. The gain mask is indicated in dotted black. . . . .   | 57 |
| 6.15 | Axial ratio, upper plot, and cross-polar discrimination, lower plot, for RX band frequencies of the proposed RHCP TLGA. The presented results are averaged for all phi cuts to better illustrate different behaviours across the band. . . . .   | 58 |
| 6.16 | Axial ratio, upper plot, and cross-polar discrimination, lower plot, for TX band frequencies of the proposed RHCP TLGA. The presented results are averaged for all phi cuts to better illustrate different behaviours across the band. . . . .   | 58 |
| 6.17 | Simulated reflection coefficient for the circularly polarized TLGA. The blue and red dots indicate the TX and RX band frequencies respectively. The black dots are simulated values outside the used bands. . . . .  | 59 |
| 6.18 | Electrical model of the final circularly polarized dual band antenna. The upper figure is the full 3D model whereas the lower plot is a, slightly tilted, cutting plane. . . . .   | 61 |
| 6.19 | The cross-polar discrimination is shown for a large band, from 7.3 to 8.3 GHz, for the RCHP TLGA. The displayed plots are averaged for all phi cuts, a small omni-variation can be expected due to non-symmetries in polarizer. . . . .  | 62 |
| 6.20 | The lower plot displays the beam pattern of the co-polarization, i.e. RHCP, of the biconical horn for the frequency range 7.3 to 8.3 GHz. The top plot displays the same information as the lower plot but in a more narrow band around the center frequency. The plots can be used as reference for how well the antenna would be able to perform in single band operation. . . . . | 63 |

# List of Tables

|     |   |    |
|-----|---|----|
| 1.1 | Commonly used frequency bands for TT&C communication on spacecrafts. The presented TLGA will be designed for deep-space X-Band communication but the design is scale-able to other bands. . . . .   | 5  |
| 2.1 | The profile options that are considered for the biconical horn antenna. I.e. linear, tangential, sinusoidal, parabolic and exponential. Note that two different orders of the sinusoidal profile will be investigated and treated. . . . .  | 17 |
| 4.1 | Specification example for vibration analysis. Vibration analysis should be performed prior to all launches of a spacecraft system. Note that the actual values will be different for a space antenna with e.g. significantly higher amplitudes. The values are only supposed to act as an illustration for the type of analysis the mechanical engineer will work with in a space antenna designs. . . . .  | 28 |
| 6.1 | Profile coordinates of the biconical horn for the optimization run displayed in Figure 6.5. The nominal value corresponds to the initial profile, the upper and lower values are the maximum and minimum values that are allowed in the optimization process. In this case the numerical points of the profile have a freedom of 5 percent. The profile coordinates are illustrated in Figure 2.1 where we now define a global Cartesian coordinate system that is located in the center between the upper and lower cone. Note that the minimum values $HP\_XMIN$ and $HP\_ZMIN$ , corresponding to $\frac{D}{2}$ and $\frac{G}{2}$ respectively in Figure 2.1, are fixed and not optimized. . . . . | 47 |
| 6.2 | Comparison table of the requirements versus the simulated values for the presented vertically polarized spline-optimized TLGA. Note that the simulated values are directivity. . . . .  | 50 |
| 6.3 | Parameters for the three layer, plane, meander line polarizer using a FR4 substrate with a relative permittivity of 4.4 and thickness (t) of about 12 mil. The parameters are illustrated in Figures 3.2 to 3.4. The layer spacing (s) is 9.180 mm. . . . .   | 50 |

|     |  |    |
|-----|--|----|
| 6.4 | Parameters for the three layer, cylindrical, meander line polarizer using a FR4 substrate with a relative permittivity of 4.4 and thickness (t) of about 12 mil. The parameters are illustrated in Figures 3.2 to 3.4. The layer spacing (s) is 9.180 mm. The three layers are displayed in Figure 6.12 which are wrapped using the rhombic shaped plane in Figure 6.11. . . . . | 51 |
| 6.5 | Comparison table of the requirements versus the simulated values for the RHCP spline-optimized TLGA. Note that the simulated values are directivity. . . . .   | 60 |

# 1

## Introduction and Background

The story began a long, long time ago when space was so empty that even time did not exist. The universe is now full of electromagnetic waves, time itself as well as static electric and magnetic fields that unites matter and even a human thought together. Everything in this universe needs to be balanced, down to the extremely tiny atom where the static Coulomb forces have to be balanced by the centripetal force of the spinning electron. You are pulled down by gravity but the electrons in your feet and the floor repel each other and you stay put. Balance is a key element in this universe for every single thing that you see. The same thing can be said about light, we need something dark to balance it. This mysterious dark force yet remains to be explained, among a million other things, but its presence is implicitly felt every single day by each human and alien being in the universe [1].

The light side of the force has, throughout the years, gone under many different names. Nowadays, the term "light" is mostly used for the visible part of the electromagnetic spectrum, i.e. from wavelengths 390 up to about 700 nm [2]. For other biological creatures, rather than humans, the eye may be adapted to other wavelengths and the visible spectrum of light may thus be defined otherwise. Light, Radio Frequencies (RF), microwaves, ultra-violet light, x-rays and gamma-rays are all just acronyms for different parts of the electromagnetic spectrum. In the end they are fundamentally the same, i.e. oscillating electric and magnetic fields, and are only separated by the number of oscillations during a second. The number of oscillations during a second, also known as frequency, has the unit Hertz named after the German Physicist Heinrich Rudolf Hertz who was the first person that verified James Clerk Maxwell's electromagnetic theory of light during the 19th century. Maxwell was the person who unified magnetism, electricity and light in twelve beautiful equations [3]. In a potential two dimensional alternative universe they can be reduced to eight. The word beautiful is, however, a relative term and could be applied to humans, flowers or even a well designed chair. What makes Maxwell's equations beautiful is not the greek symbols, but rather what they represent and their universal meaning. Alien beings are also governed by the same physical laws and thus, if sufficiently evolved, have their version of Maxwell's equations but most likely under a different name and different mathematical methods. This is what makes Maxwell's equations beautiful. The way they unify fundamental forces of nature, are universally applicable and allow us to design and build systems. Systems that one day may allow us to shake hands with many of our, very plausible, neighbours throughout the universe.

Earth will eventually be uninhabitable, may it be through nuclear war, climate change or an asteroid impact the prosperous days of the blue planet will come to an end. Thus as stated in the sixties by Captain James T. Kirk: "Space is, and will always be, the final frontier for the human race". A full migration to an extra-terrestrial planet is, however, not something we are considering to do any time soon. We still have many amazing things and discoveries to look forward to in our, on a cosmological scale, short life span. E.g. the possibility of finding extra-terrestrial life in our solar system, receive artificial signals from outer space and to initiate the in-habitation of Mars. The 21th century may very well be the time where history books are rewritten and the very essence of being a human is disrupted. To reach the described forthcoming we need to develop the systems of the future. In explicit; we need new systems that can meet and handle all the prospective challenges. One such system is the space antenna and the associated front and back-end components [4].

### 1.1 Telemetry, Tracking and Command Spacecraft Systems

Telemetry, Tracking and Command (TT&C) systems are an essential element in satellite communications and provide many of the basic functions required for a spacecraft such as to [4][5]

- Process received commands
- Handle basic satellite telemetry
  - System status messages (e.g. on/off)
  - System temperatures
  - Gain settings for the transponders
  - Status parameters of amplifiers
  - Pointing position of antennas
- Support ground stations, for example in range determination
- Support satellite control functions
  - Attitude determination and control
  - Battery charge management and solar array pointing
  - Autonomous configuration management

Many of these functions need to be accessible at all times during the operational life span of the satellite. However, in some cases the orientation of the satellite is not always known, such as during launches, transfer orbits and e.g. during on-orbit attitude anomalies. Consequently a full sphere of coverage around the satellite is required for the TT&C communication system. Low Gain Antennas (LGAs) are used to solve the problem and are, as to this date, the only way to achieve full TT&C functionality for a spacecraft. Let us first take a look at the TT&C back-end systems, i.e. the components behind the antennas before we proceed with a closer look at the antenna configurations.

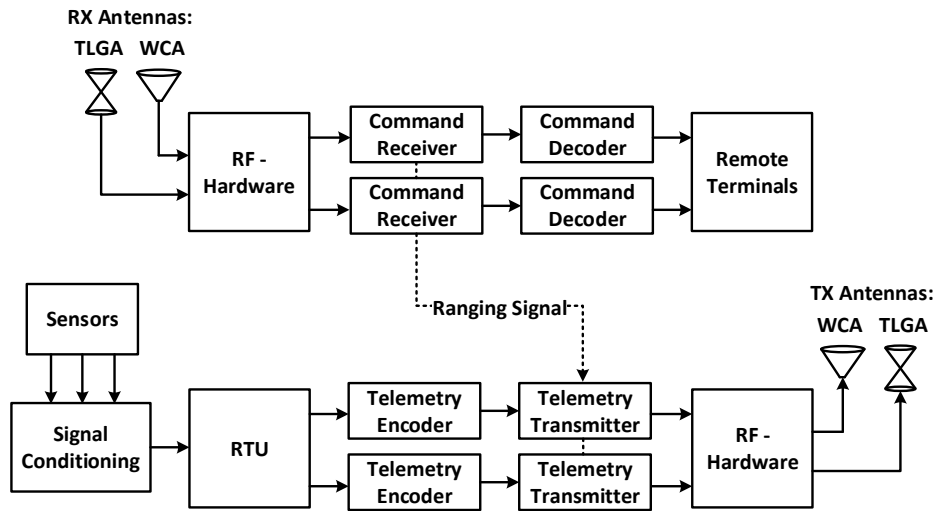


**Figure 1.1:** Simplified system architecture for satellite TT&C communication. The upper and lower diagram display the receiving and transmitting chain respectively.

### 1.1.1 TT&C Back-ends

The differentiation between front and back-end is no longer well defined with the introduction of e.g. Software Defined Radios (SDR) [6][7]. Antennas and components such as the Low Noise Amplifier (LNA) are still clearly associated with the front-end and will not find a replacement in software any time soon. However, other dedicated hardware functions, such as circuits for auto-correlation, filtering and RF-mixing, can be defined and programmed in software, opening new possibilities in satellite communications. The cost-effectiveness of a digital solution is, in general, very high in comparison to a hardware solution. Furthermore, the flexibility of SDRs are another great advantage allowing satellite suppliers to update, already launched, satellites with new features and change e.g. bandwidths to meet specific customer demands [8]. SDR systems can be made very compact and thus be very beneficial for e.g. small satellite platforms. This has been shown for equivalent ground based systems by the author of this thesis [9].

A system architecture for a TT&C system is presented in Figure 1.1. The architecture is based on the block diagrams provided in [5] but with slight modifications. Note that Figure 1.1 is simplified and the purpose is only to give an overview of the workings of a satellite TT&C system. The upper and lower diagram displays the receiving and transmitting TT&C chain respectively. A number of different sensors are used on the spacecraft, the sensor reads e.g. all basic telemetry as outlined in the introduction of this chapter. The signals are assessed and relayed to a microprocessor i.e. the Remote Terminal Unit (RTU) and coded onto carrier waves transmitted by antennas. For the receiving chain the antennas are always followed by an LNA and other components such as mixers. The commands are subsequently decoded and interpreted by a microprocessor to perform the desired action, such as solar array pointing.

### 1.1.2 Antenna Configurations

There exists two basic antenna configurations for TT&C systems [5]. Firstly, we have a variant mainly used by European satellite suppliers where two very low gain Wide Coverage Antennas (WCA) are used to cover the full sphere around the satellite. The second option is to use two WCAs in conjunction with a TLGA. The latter option, used by North American satellite suppliers, is displayed in Figure 1.2 where the two WCAs are illustrated as reflectors and the TLGA as the red bicone. The WCAs are commonly low gain horns or helices whereas the TLGA is, in almost all cases, a biconical horn. The exception for the latter is in cases where the electrical and mechanical requirements are a lot less strict, such as for a Cubesats where a simple monopole could be used. Furthermore, the TLGA will provide the azimuthal coverage, or the toroidal coverage, around the satellite. The most common frequency bands for TT&C antennas are listed in Table 1.1.

It must be emphasised, that while the two described configurations are the most common for a satellite, some missions have more strict requirements. For example in deep-space spacecrafts, having two or three antennas for the full sphere of coverage may not be sufficient due to high gain requirements. One example is the Juno mission to Jupiter where a total of five antennas were used [10]. It was calculated that a peak gain greater than 4.5 and 6.0 dBi, for the TX and RX band respectively, was required in the azimuthal plane of the spacecraft. This requirement can only be satisfied by employing an omnidirectional antenna.

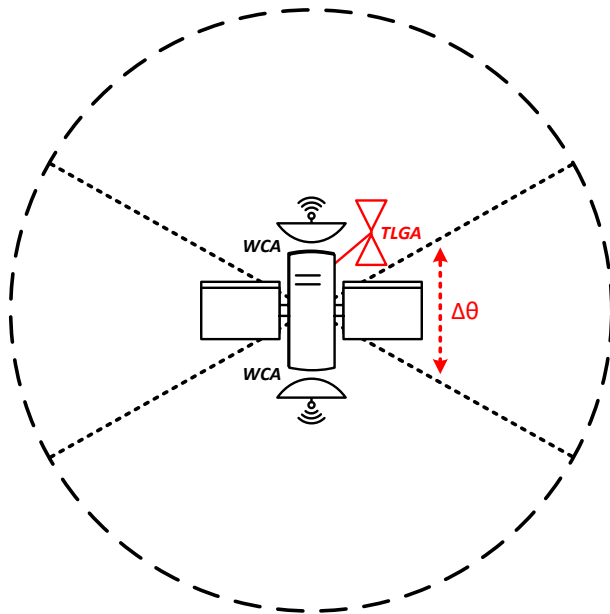


**Figure 1.2:** Illustration of the most common TT&C antenna system used by North American satellite suppliers. Two Wide Coverage Antennas (WCAs) are used in combination with a Toroidal Low Gain Antenna (TLGA) to provide full coverage around the satellite.

**Table 1.1:** Commonly used frequency bands for TT&C communication on spacecrafts. The presented TLGA will be designed for deep-space X-Band communication but the design is scale-able to other bands.

| Frequency Band              | Uplink (MHz)               | Downlink (MHz)             |
|-----------------------------|----------------------------|----------------------------|
| <i>S – Band</i>             | 2025 - 2110                | 2200 - 2290                |
|                             | 2110 - 2120 (Deep-Space)   | 2290 - 2300 (Deep-Space)   |
| <i>X – Band</i>             | 7190 - 7235                | 8400 - 8450                |
|                             | 7145 - 7190 (Deep-Space)   | 8450 - 8500 (Deep-Space)   |
| <i>K<sub>u</sub> – Band</i> | 16600 - 17100              | 14400 - 14470              |
| <i>K<sub>a</sub> – Band</i> | 40000 - 40500              | 37000 - 38000              |
|                             | 34200 - 34700 (Deep-Space) | 31800 - 32300 (Deep-Space) |

## 1.2 Toroidal Coverage Antennas

Toroidal coverage antennas are omnidirectional antennas i.e. they radiate equally in all directions in an azimuthal plane as illustrated in Figure 1.3. Note that the illustration is an ideal case where no ripples or side lobes are present. A toroidal shaped beam can be obtained from a number of different antennas [11]. The most fundamental antenna is the dipole, consisting of a simple wire with a length of  $\frac{\lambda}{2}$  at the design frequency. If we instead shape and cut the dipole wire another omnidirectional antenna emerges known as the cloverleaf antenna. Many other different variations of the dipole exist, such as the Lindenblad antenna. The omnidirectional pattern can also be obtained from monopoles, loops or e.g. patches on a cylinder. A general problem with these topologies are that they suffer from low efficiency and bandwidth. Breakdown due to multipaction could also become a problem [10]. An interesting topology for a TLGA is the normal-mode mono or multifilar helix. The problem here, once again, is narrow bandwidth and low efficiency and it would almost certainly never be able to act as a dual band antenna for e.g. deep space TT&C communication using a single element. A two element design, e.g. in a parasite configuration, helix could solve the problem. The topology may be interesting, if the problems can be dealt with using new creative methods, for another thesis on TLGAs.

Continuing with the variants of the dipole we find one very interesting topology, i.e. the biconical horn. The biconical horn can be thought of as a dipole but where the two poles instead have the shape of linear cones. The bicone configuration effectively extends the bandwidth of the dipole, up to several octaves. Furthermore, the geometry is more mechanically robust and the radiation pattern and gain can be shaped and controlled to a much larger extent in comparison to a wire antenna. These are some of the reasons why biconical horns are the predominant choice for spacecrafts. Several biconical TLGAs have been proposed and used on spacecraft systems throughout the years. RUAG Space is an international company supplying state-of-the-art satellite equipment to different satellite manufacturers around the world [12] [13]. Their latest toroidal antenna, developed for *K<sub>u</sub> – Band*, is shown in Figure 1.4 [14]. It is a biconical type horn antenna using a stacked element con-

figuration with the RX antenna at the top, i.e. the small bicone, and the larger TX antenna just below. In general, the transmitting antenna of a satellite has lower frequency in comparison to the receiving band, hence the difference in size. Note that this is not always the case such as for TT&C X-Band links, refer to Table 1.1. The RUAG Space antenna is excited by an array slots using cylindrical waveguides and septum polarizers. To excite the waveguides of the upper bicone, coaxial cables are used which has to be carefully routed to minimise the influence on the radiation patterns. Another biconical horn that was developed for space, by the company Rymasa, is presented in [15]. The configuration with the dual bicone, one for RX and one for TX, is similar but the feeding is different using a turnstile junction. One can quickly see that these antennas are complex, hard to manufacture and thus very expensive. A large step forward, in the development of bicone antennas was taken by NASA Jet Propulsion Laboratory (NASA JPL), where a new design was proposed [10]. The presented antenna was a single element bicone, used for dual band TT&C communication at X-Band, using a simple TEM excitation where a coaxial conductor connects to upper and lower cone. To meet the gain and size requirements for the TLGA, JPL used a parabolic shaped profile instead of the typical linear variant. A four layer polarizer, of meander type, was furthermore used and corrugations were employed to reduce side lobe levels. The JPL design has been a great source of inspiration in this thesis.

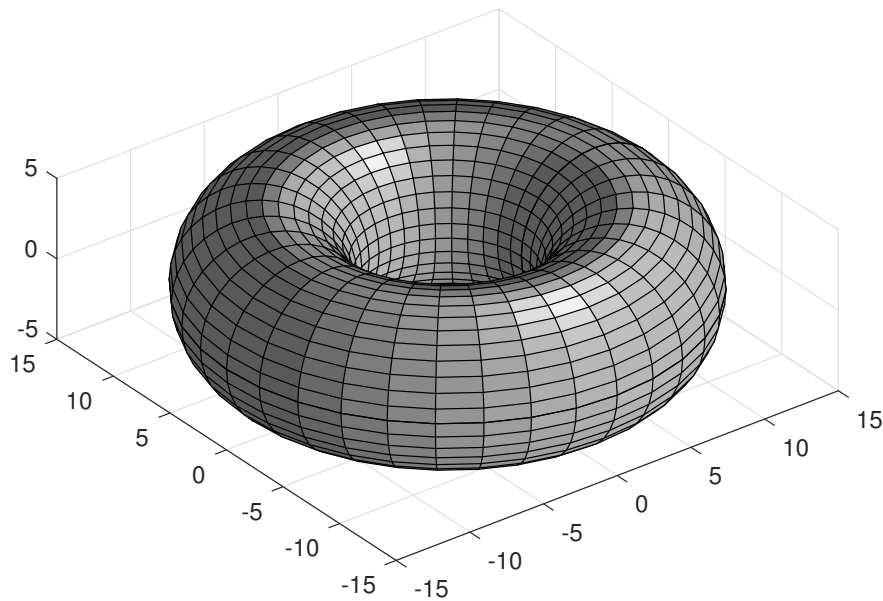


**Figure 1.3:** Illustration of a toroidal shaped beam pattern as radiated from e.g. a biconical horn antenna positioned vertically in the center of the toroid.



**Figure 1.4:** A Toroidal Low Gain Antenna (TLGA) developed by RUAG Space AB for  $K_u$ -Band. The main antenna elements are two bicones, fed by an array of slots using cylindrical waveguides and septum polarizers. The upper (smaller) bicone is the RX antenna element and the lower is the TX.

### 1.3 Thesis Organization and Scope

This thesis treats the electrical design and simulations of a dual band, single element, circularly polarized biconical horn. The presented antenna should not be viewed as new topology in itself but rather as a significant evolution of the biconical horn. We also want to emphasise that the thesis is not about developing new theories or to provide a theoretical foundation for each single element that will be discussed. It is about practical design and how we can modernize antennas, where many have existed unchanged for almost 100 years, using computational power and design methods that have been introduced in the 21st century. Deep mathematical formulations will also be avoided as much as possible, instead emphasis is put on intuition, understanding and actual behaviour of the considered antenna.

A theoretical foundation for the biconical antenna is provided in the second chapter of the thesis, where one significant difference from classical authors on bicones, are the profile options and design curves using contours. Fundamental theory of meander-line polarizers are outlined in chapter three where we explain the workings using a very elegant Smith Chart approach. Mechanical and thermal design, and the corresponding results, are outside the scope of this thesis. It must be noted that the design procedure of a spacecraft antenna is, undoubtedly, very different from an ordinary ground based antenna. Firstly, the antenna needs to survive the launch of the spacecraft and secondly it must endure the harsh environment of space.

However, in order for the antenna to meet the strict requirements, the effects must be considered for in the electrical design of the antenna. We have dedicated chapter four for requirements and specifications so the reader can get an overview of the complexity in designing an antenna for space. The electromagnetic parts of chapter four contain the requirements we will try to meet using a new approach in the design of biconical horns. The methods are outlined in chapter five. Chapter six contains the results of the electrical simulations. The results will be divided into five main sections where the first will treat the selection of the biconical horn profile. Section two shows the antenna characteristics with no polarizing structure i.e. a vertically polarized TLGA. In section three, the results of a designed three layer meander type polarizer are presented. The two final sections of chapter six are dedicated to the circularly polarized antenna design. The thesis is finalized with discussions and conclusions in chapter seven.

# 2

## Biconical Horn Antennas

In this chapter we will present fundamental theory of biconical horn antennas. We will discuss mode content and how to quickly determine the geometry of a bicone antenna using directivity design curves. Furthermore, we will treat the antenna as a horn to derive the E-plane pattern. Input impedance, profile options, feeding techniques and corrugations will also be discussed. The presented content on biconical horns is based on books from authors that are very well known in the antenna community i.e. [5], [11], [16], [17], [18] and [19]. The section also relies on three classic articles from Papas, King and Barrow who were among the first to extensively analyze the bicone antenna [20] [21] [22]. Note that some equations have been rewritten with different notations and formulations.

### 2.1 Mode Content and Directivity Design Curves

The two first modes of the bicone antenna are the TEM and  $TE_{01}$  modes respectively. These are also the most useful modes providing a toroidal shaped beam. The outward propagating waves can be described as spherical for the straight profile bicone antenna whose geometry is displayed in Figure 2.1. Several higher order modes can be excited if the conditions are right but the radiation pattern is not omnidirectional for these cases. The higher order mode conditions may be fulfilled if e.g. the gap size,  $G$  in Figure 2.1, is very large in terms of the wavelength. Using a coaxial line as feeding element, where the inner conductor connects to the upper cone and the outer to the lower, the useful TEM mode is excited. The electric field lines of course obeys Maxwells equations and are perpendicular to the cone profile and directed along the axis of the cone. The polarisation vector is thus vertical and the cross-polarization is, ideally, zero as well as the azimuth ripple.

The  $TE_{01}$  mode can be excited in several ways. One common way is to use an array of slots, placed around a cylinder. It is also possible to use an array of dipoles or a small loop in the gap between the cones to excite the mode. The  $TE_{01}$  mode requires a distance between the cones of at least  $\frac{\lambda}{2}$  and it will provide horizontal polarization. Since we have an array of elements in the azimuthal plane, azimuth ripple can be expected which is undesired for a space TLGA. We can directly conclude that the  $TE_{01}$  mode design will be a lot more mechanically complex, harder to manufacture, will be larger and have a undesired azimuth ripple in contrast to a coaxially fed TEM design. A great benefit that it presents to a space antenna is the structural stability, which is also the reason why it's so commonly used.

This can be solved for the TEM excited horn by using stabilizing structures such as layers of meander-line polarizer as shown in e.g. [10].

There are many different approaches to derive the fields and thus the directivity of the bicone antenna. The fundamental way is to apply Maxwells equations, restrained by the boundary conditions for the conductors. The analytic expressions of the fields can be found in e.g. [22]. Studying the E-plane pattern, we notice that it actually looks almost exactly as the fields of a sectoral horn. This has been noted by several authors throughout the years. Thus we can view the bicone antenna as both a broadband dipole and a horn. For small cone angles the dipole characteristics will, however, dominate and vice versa for large angles. The viewpoint of the bicone antenna as a horn is very interesting and it will be treated as such for the remainder of the thesis.

Due to the rotational symmetry of the horn, and viewing the bicone as a cylindrical aperture, the directivity will be proportional to the distance between the endpoints of the cone which will be referred to as the aperture height i.e.  $H$  in Figure 2.1. More explicitly it is limited by the expression  $\frac{2H}{\lambda}$ . However, Amplitude Taper Losses (ATL) and Phase Error Losses (PEL) are present which will effectively reduce the directivity of the horn according to

$$D_{dB} = 10\log\left(\frac{2H}{\lambda}\right) - PEL_{dB} - ATL_{dB} \quad (2.1)$$

The ATL is approximately 0.91 dB for the  $TE_{01}$  mode since it has a cosine field distribution. For the TEM mode the ATL is zero due to its uniform distribution. The PEL for the  $TE_{01}$  and TEM mode respectively can be calculated using the field distribution together with the quadratic phase distribution constant

$$S = \frac{H^2}{8\lambda K} \quad (2.2)$$

where  $K$  is the slant radius of the biconical horn which we define as

$$K = \sqrt{R^2 + \left(\frac{H}{2}\right)^2} \quad (2.3)$$

or equivalently using the cone angle  $\Phi_0 = \arctan\left(\frac{H}{2R}\right)$

$$K = \frac{H}{2\sin(\Phi_0)} = \frac{R}{\cos(\Phi_0)} \quad (2.4)$$

$H$  is the aperture height and  $R$  the cone radius as shown in Figure 2.1. The quadratic phase distribution constant can be interpreted as a measure of the radial phase error at the aperture. Increasing the aperture height will induce a larger phase error and the directivity will be reduced. The directivity is also directly proportional to the aperture height, as shown by equation 2.1. Consequently there must exist an optimal antenna geometry, directivity wise, as defined by the cone radius and aperture height of the bicone. This is displayed in Figure 2.2 which is a plot of equation 2.1 where the radius is constant for each curve and the aperture height is swept. E.g. for

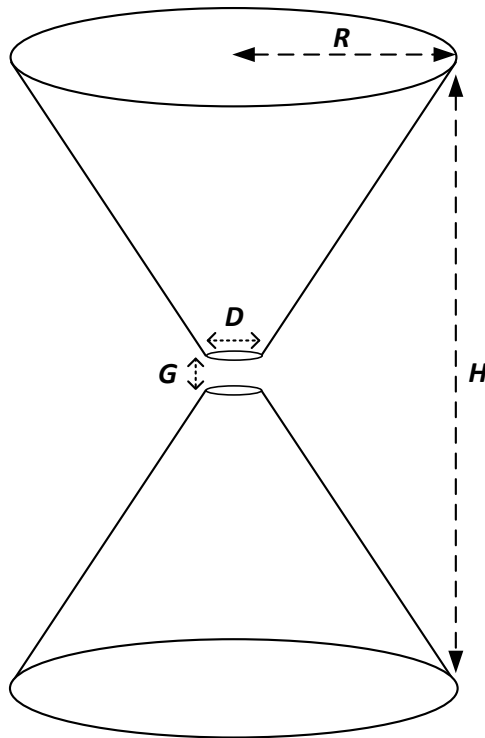


**Figure 2.1:** Geometry for a straight profile biconical horn.  $H$  denotes the aperture height,  $R$  the cone radius or antenna radius,  $D$  is the diameter of the gap and  $G$  the gap size.

a cone radius of one wavelength and an aperture height of about  $1.8 \lambda_0$  we find the optimal antenna geometry with respect to the directivity. These curves are very useful for the design of straight profile biconical horns. From the plots we can quickly determine the geometry and thus the size of the antenna for a desired directivity at the beam center.

Another useful way to illustrate the directivity of the horn is through contour plots as shown in Figure 2.3. The displayed contour plot represents a directivity grid for different cone and aperture height values along the  $x$  and  $y$  axis respectively. I.e. the intensity of the contour plot displays the directivity at the beam center or, in the spherical coordinate system, the directivity at  $\theta = 90^\circ$ . Note that if we set the cone radius constant, in the contour plot, and plot the directivity versus the aperture height we obtain the same plot as in Figure 2.2. The usefulness of the contour plot is not only that it provides a more general form of the curves displayed in Figure 2.3, but also that it presents information on the gain variation over a specified bandwidth. The plots of Figure 2.2 are in contrast very useful when fast sweeps, with the purpose of finding the optimum antenna for a constant cone radius, are desired. Let us first quickly recap the definition of bandwidth before we proceed with a design example using the contour plots. Let  $f_H$  denote the highest frequency of the band and  $f_L$  the lower. The center frequency is commonly defined as the

arithmetic mean of  $f_H$  and  $f_L$  but the geometric mean is also used. We will use the latter definition and thus  $f_c = \sqrt{f_H f_L}$ . One definition for the bandwidth is in percentage according to

$$B[\%] = 100 * \frac{f_H - f_L}{f_c} = 100 * \frac{f_H - f_L}{\sqrt{f_H f_L}} \quad (2.5)$$

The more common definition for a wideband antenna is to instead express the bandwidth as a ratio

$$(B = \frac{f_H}{f_L}) \implies (B : 1) \textit{Bandwidth} \quad (2.6)$$

Let us consider the design of a straight profile biconical horn where the directivity and it's variation over a specified bandwidth are two important figure of merits. For example, let the straight profile bicone have a center frequency ( $f_0$ ), corresponding to free space wavelength ( $\lambda_0$ ), and select the optimum aperture height for a cone radius of one wavelength in Figure 2.2. The bicone antenna will have an aperture height of approximately  $1.8\lambda_0$ . At the design frequency we can expect a directivity of approximately 4 dB. In this example we let the upper frequency in the band be 10 GHz and the lower 8 GHz, then the center frequency is approximately  $f_c = 8.94GHz$  and the bandwidth about 22 percent. The bicone geometry is furthermore defined at the center frequency i.e. we let the aperture height be equal to  $1.8\lambda_0 = 1.8\lambda_c$  where  $\lambda_c$  corresponds to the frequency  $f_c$ . The radius of the bicone is also defined at the center frequency i.e.  $1\lambda_c$ . Since the wavelength is smaller at the upper part of the band, and higher at the lower part of the band, the bicone will be larger and smaller respectively in terms of the wavelength. More explicitly, the aperture height at the upper part of the band will be  $\frac{1.8\lambda_c}{\lambda_u} = 2.0\lambda_u$  and the cone radius  $\frac{1\lambda_c}{\lambda_h} = 1.12\lambda_h$ . The same method can be applied to the lower part of the band. Finally, by reading the corresponding directivity values from the contour plot in Figure 2.3 the directivity variation can be determined.

## 2.2 Azimuth and Elevation Patterns

The E-Plane pattern, or the elevation pattern, of the biconical antenna can be derived from Maxwell equations as shown in e.g. [22] and discussed in section 2.1. The azimuth pattern is ideally at a constant level for a given  $\theta$  angle due to rotational symmetry.

The E-Plane pattern of a sectoral horn, or a biconical horn, is shown in Figure 2.4 for several different phase errors. The y axis displays the relative level of the E-plane pattern in dB as a function of the elevation angle  $\theta$ . The aperture phase error (S) is defined in equation 2.2 and it is directly proportional to the geometry of the bicone. As seen in Figure 2.4, as the phase error increases the directivity is reduced while the side-lobe levels increase. The goal is to keep the phase error as low as possible if high directivity and low side-lobe levels are desired.

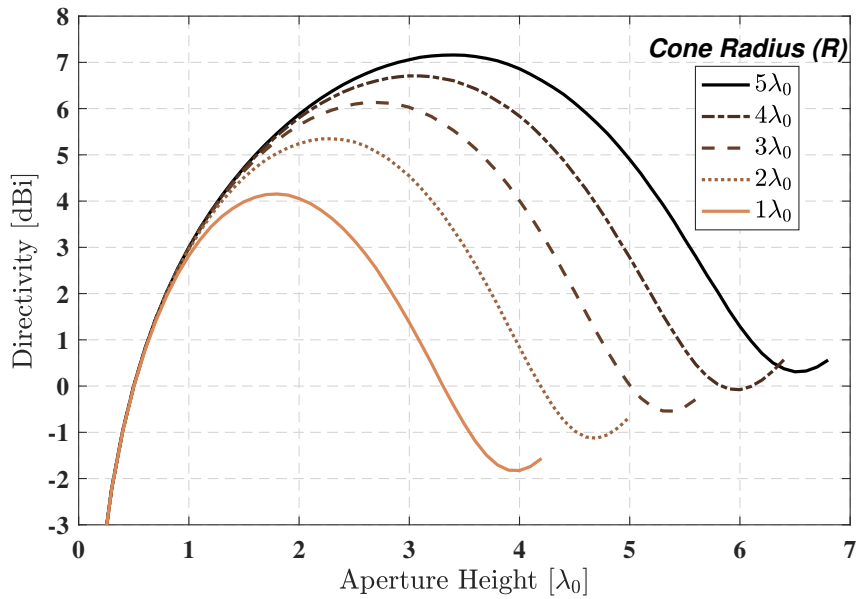


**Figure 2.2:** Theoretical directivity as a function of the aperture height for a straight profile biconical horn. For each directivity curve the cone radius is constant and linearly increasing from one free space wavelength ( $\lambda_0$ ) to five.

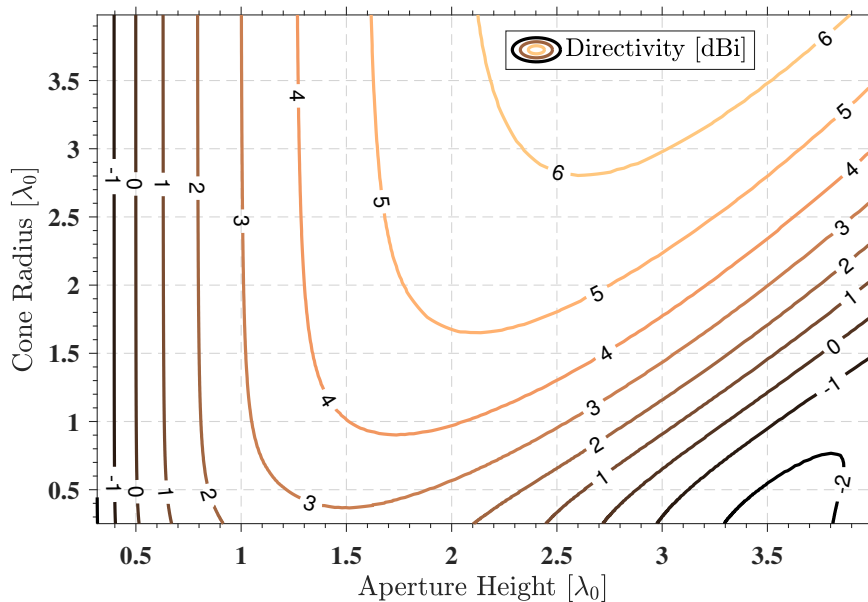


**Figure 2.3:** Directivity contour plots for a straight profile biconical horn. The contour plot can be useful to find optimal antenna geometries, in terms of the cone radius and aperture height. Furthermore, it can provide information on the gain variation over a specified bandwidth.

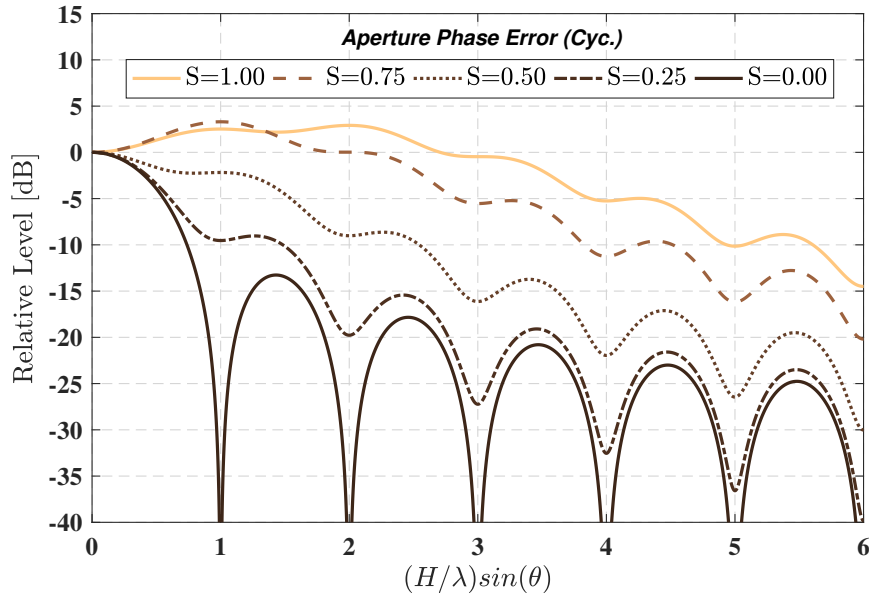


**Figure 2.4:** Relative E plane pattern of a sectoral horn for different aperture phase error ( $S$ ). The E plane pattern of a sectoral horn corresponds, in good approximation, to the E plane pattern of a biconical horn.

A trade-off may be required if a wide beam, i.e. lower directivity, is a figure of merit in the design. The antenna geometries as defined by the design curves in Figure 2.2 and 2.3 are directly associated with phase error as discussed in 2.1. E.g. selecting the geometry of the example in section 2.1, i.e. an aperture height of  $1.8\lambda_0$  and a cone radius of  $1.0\lambda_0$ , yields the phase error  $S = 0.3$  cycles. We can proceed to determine the shape of the E-plane, the side-lobe levels and beam width using Figure 2.4.

## 2.3 Input Impedance

Consider the case of a TEM excited biconical horn with cone radius  $R$  and cone angle  $\Phi_0 = \arctan(\frac{H}{2R})$  as illustrated in Figure 2.1. We can then express the input impedance as

$$Z_{in} = Z_0 \frac{1 - \frac{\beta}{\alpha}}{1 + \frac{\beta}{\alpha}} \quad (2.7)$$

Where the characteristic impedance  $Z_0$  is

$$Z_0 = 60 \ln\left(\cot\left(\frac{\Phi_0}{2}\right)\right) \quad (2.8)$$

The relation was derived using a mathematical hemisphere that represents a boundary between the reflected TEM wave and the transmitted wave. The ratio is expressed as  $\frac{\beta}{\alpha}$  which follows the relation

$$\frac{\beta}{\alpha} = e^{-2ika} \frac{1 + \frac{60i}{Z_0} \sum_{i=1}^n \frac{2n+1}{n(n+1)} [P_n(\cos(\Phi_0))]^2 \zeta(ka)}{-1 + \frac{60i}{Z_0} \sum_{i=1}^n \frac{2n+1}{n(n+1)} [P_n(\cos(\Phi_0))]^2 \zeta(ka)} \quad (2.9)$$

$P_n$  is Legendre polynomial of order  $n$ , note that the summation is only valid for odd  $n$ :s.  $\zeta(ka)$  is a complex auxiliary function which is equal to

$$\zeta(ka) = \frac{h_n^{(2)}(ka)}{h_{n-1}^{(2)}(ka) - \frac{n}{ka}h_n^{(2)}(ka)} \quad (2.10)$$

The spherical Hankel of the second kind i.e.  $h_n^{(2)}(ka)$  can be calculated using Matlab toolboxes, ordinary summation in Matlab or by hand. The latter option is, however, not recommended unless time is not of the essence but it can be a fun practice. Using equations 2.7 to 2.10 we can proceed to calculate the input impedance of the antenna as shown in Figure 2.5. The figure displays the characteristic impedance ( $Z_0$ ), the input resistance and the imaginary part of the impedance i.e. the reactance. The cone angle ( $\Phi_0$ ) is set to a constant value of 50 degrees and the cone slant range,  $K$  in equation 2.3, is swept from zero to four normalised wavelengths. From the plot we see that the input impedance will be constant for a constant cone angle and the input impedance is frequency independent. Furthermore, the input resistance will converge towards the characteristic impedance of the bicone if the cone slant range approaches infinity. For a finite slant range there are slight deviations from the characteristic impedance but often the characteristic impedance, defined in equation 2.8, is a sufficient initial value for the geometric design of the antenna. By varying the cone angle we can quite easily match the bicone to a 50  $\Omega$  transmission line i.e., if designed correctly, it can be directly fed with a 50  $\Omega$  coaxial feed. Knowledge of what is a decent cone angle, if a matching stage is to be avoided, will be important in the profile investigation where we aim to find a suitable antenna that can operate as a simultaneous RX and TX TLGA.

Theory is extremely important but reality always looks different, we believe this is important to emphasise even in the theory part of the thesis. Thus we present what the input resistance of a biconical horn actually would be if we measured it using sophisticated instrumentation such as an EM simulation tool in Figure 2.6. The plot displays input resistance, where the aperture height is swept over a constant range, resulting in a plot with resistance versus cone angles for different cases of cone radius and gap sizes. A theoretical plot, in dotted black, of equation 2.8 is also displayed. From the plot we can observe that the input resistance is dependent on the gap size, as already mentioned, as well as the cone radius. Thus, it does not only depend on the cone angle as stated in theory. It will actually also depend on both the aperture height and the gap diameter i.e  $H$  and  $D$  respectively in Figure 2.1.

## 2.4 Profile Options

A feed-horn, corrugated or smooth walled, commonly use an analytical profile in the design. Different analytical profiles for horn antennas such as elliptical, exponential, power of variables, power of tangential, power of hyperbolic, power of asymmetric sine-squared and so forth have been extensively investigated in e.g. [23] by Christophe Granet.

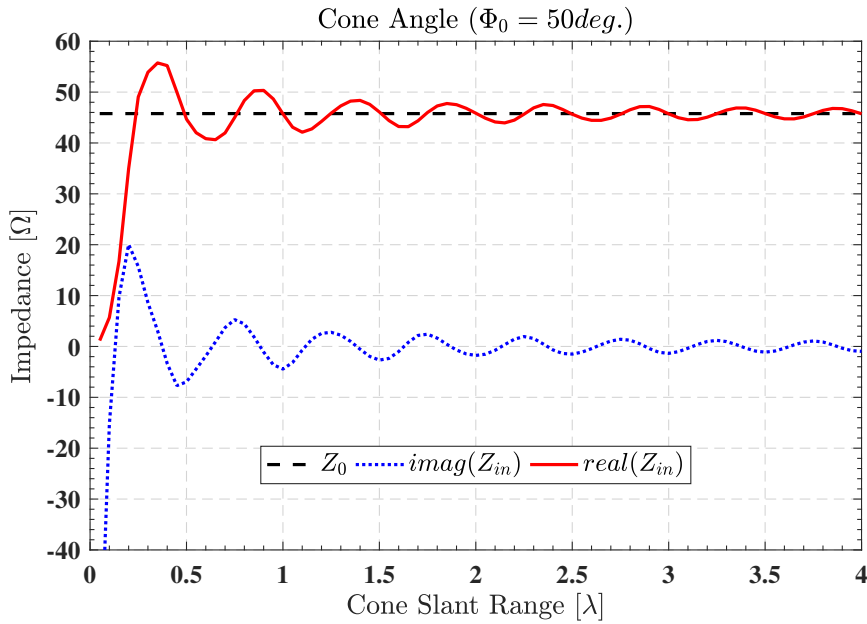


**Figure 2.5:** Input impedance, reactance in blue and resistance in red, of a biconical horn antenna for a constant cone angle of 50 degrees. The characteristic impedance ( $Z_0$ ) of the antenna is displayed in black.

Profiling the horn antenna has a large impact on the radiation pattern and it is extremely important to select the correct profile for the specifications at hand. The profile greatly affects e.g. the side-lobes of the antenna as well as the cross-polar levels. Another major advantage is that the size of the horn can be reduced while maintaining the same performance.

By viewing the biconical antenna as a horn, as discussed in section 2.1, we open the possibility of finding new high performing omnidirectional antennas. Some work has been done on profiles for the biconical horn but in a very limited sense in comparison to feed-horns. E.g. the vertical parabolic shaped bicone in [14], by RUAG Space, and the horizontal parabolic shaped antenna by NASA JPL in [10] used on the Juno spacecraft. JPL found that a parabolic shaped bicone antenna could maintain the high gain requirements while using smaller dimensions in comparison to a straight profile design.

Some of the commonly used analytical profiles are outlined in [23]. Modified versions as well as new additions are presented in [24] where the different profiles were applied to the Quad Ridge Flared Horn (QRFH) [25]. The profiles that will be considered for the proposed bicone antennas are slightly modified versions of those presented in [23]. To limit the search space, six profiles, including two sinusoids, will be investigated as outlined by Table 2.1. Note that the variables  $x$  and  $r$  in Table 2.1 can be exchanged for more profile options but we will not treat these cases. Referring to Table 2.1 we will only consider profiles of the second order and the linear taper, as specified by the variable  $A$ , will be set to one to limit the analysis. The previous statements excludes the sinusoidal profile where we will also investigate the

case of a fourth order function and a linear taper of  $A=0.5$ .

The profiles are displayed in Figure 2.7. The profiles will be rotated around the vertical axis and extruded in horizontal plane to complete the biconical horn. The purpose of the investigation, as defined in scope of the thesis in section 1.3, is to find an antenna that meets the requirement to function as both a TX and RX antenna. Another main goal is to find a good initial profile for numerical profile optimization. The results will be presented in section 6 where we will evaluate side-lobes, directivity, beam width and mechanical viability of the profiles.

**Table 2.1:** The profile options that are considered for the biconical horn antenna. I.e. linear, tangential, sinusoidal, parabolic and exponential. Note that two different orders of the sinusoidal profile will be investigated and treated.

| <i>Profile Name:</i>      | <i>Expression:</i>   |
|---------------------------|--|
| <b><i>Linear</i></b>      | $r(x) = r_i + (r_o - r_i)\frac{x}{D}$                                      |
| <b><i>Tangential</i></b>  | $r(x) = r_i + (r_o - r_i)[(1 - A)\frac{x}{D} + A\tan^p(\frac{\pi x}{4D})]$ |
| <b><i>Sinusoid</i></b>    | $r(x) = r_i + (r_o - r_i)[(1 - A)\frac{x}{D} + A\sin^p(\frac{\pi x}{2D})]$ |
| <b><i>Parabolic</i></b>   | $r(x) = r_i + (r_o - r_i)[(1 - A)\frac{x}{D} + A(\frac{x}{D})^p]$          |
| <b><i>Exponential</i></b> | $r(x) = r_i \exp(\ln(\frac{r_o}{r_i})\frac{x}{D})$                         |

## 2.5 Corrugations

The main goal with an antenna is to direct electromagnetic radiation in a predetermined direction. Thus, at least for a TLGA, we want all the energy in the main lobe. Side lobes are unavoidable parasites in the radiation pattern and are very undesired. Corrugations are commonly used for toroidal coverage space antennas to reduce the side lobe levels [10] [12] [13] [14] [15]. There are several parameters that are required to fully define the geometry of the corrugations. Firstly, the width and depth of the corrugations. Secondly, the number of corrugations as well as the thicknesses are also of great importance. The width and depth are, in almost all cases, defined in terms of the wavelength used in the design. Corrugations may also be designed to act as either a hard or a soft surface [16]. Manufacturing wise, corrugations require very precise and complex machinery and thus it often renders a very expensive antenna. Using computational power in combination with advanced algorithms, applied on a smooth profile, can eliminate the need for expensive and complex corrugations. The latter will be shown in chapter 6.

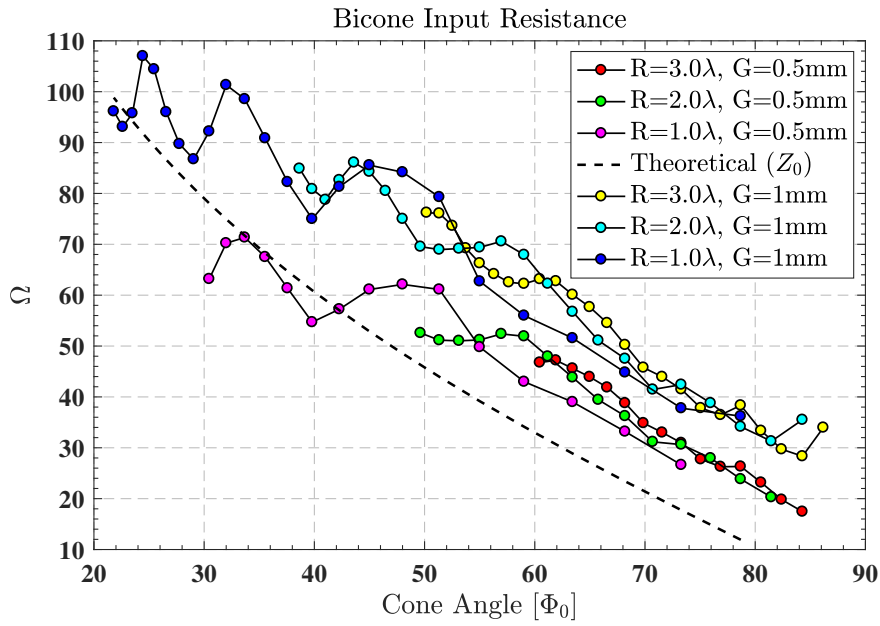


**Figure 2.6:** Actual, simulated, input resistances for TEM excited biconical horns of different antenna radii and gap sizes. The black, dotted, line displays the theoretical characteristic resistance as defined by equation 2.8.

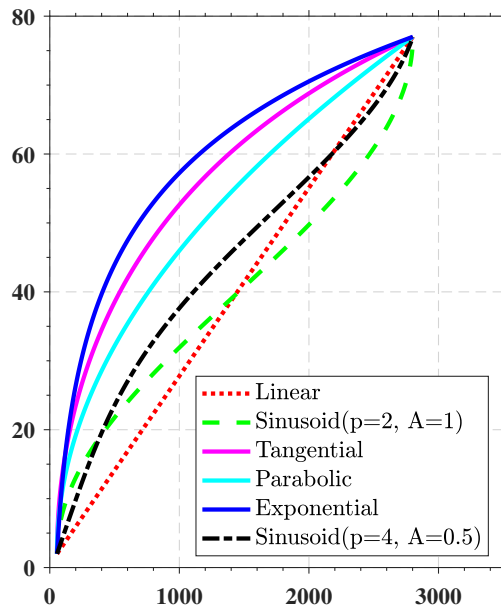


**Figure 2.7:** The profiles that will be investigated for the biconical horn. Two variants of the sinusoidal profile are considered, i.e. using two different orders ( $p$ ) and linear tapers ( $A$ ).

# 3

## Meander-Line Polarizers

The concept and the first design, using a computer program, of a meander-line polarizer was presented by scientists at Stanford Research Institute in 1966 [26]. A few years later, in 1973, a three layer polarizer was designed at  $X_{Band}$  where an axial ratio better than 1.5 dB was obtained with a very low dissipation loss on the order of 0.05 dB [27]. It was also shown that the basic design could be scaled to frequency bands in the range of 1 - 20 GHz. One problem with the polarizer is that higher angle of incidence deteriorates the performance. A solution to the problem was presented in [28] where the polarizer was optimized for oblique incidence angles. However, oblique incidence optimization relies on the use of dielectrics as a medium between the meander layers as further shown in e.g. [29]. For a space antenna, the use of dielectrics need to be minimised to avoid stacking of charge. This could pose as a problem for us later in the design due to the spherical wave front in the near field of the biconical horn.

A common design procedure for the meander-line polarizer is to compose circuit equivalents and optimize the polarizer using circuit analysis tools. A new and effective circuit model approach, using a semi-lumped equivalent, is presented in [30]. In this communication we will use a classic approach and visualise the workings of the polarizer using Smith Charts. The retrieved basic design can further be developed upon using advanced optimization algorithms and tuning. The design procedure in the first section follows a method outlined in [29]. In the second section of this chapter we propose a method for how to convert a plane polarizer to a cylindrical.

### 3.1 Design Theory

Consider a matrix, where we let the row and columns consist of a structure exhibiting inductance and capacitance respectively. If we now let a plane wave, parallel to the diagonal of the matrix, pass through the structure, the two orthogonal components of the incident wave will experience a phase shift. This is the very basic principle of single layer meander-line polarizers, where the matrix is realized as per Figure 3.3. If we continue to plot the inductance and capacitance of the meander matrix in a Smith Chart, refer to Figure 3.1, more details of the single layer polarizer can be revealed. Let the experienced inductance and capacitance of the parallel and perpendicular component of the incident field be denoted  $jX_{\parallel}$  and  $-jX_{\perp}$  respectively. If we plot the components in the Smith Chart, i.e. the blue dots in Figure 3.1, we can determine the corresponding reflection coefficients ( $\Gamma_{\parallel}$  and  $\Gamma_{\perp}$ ) by calculating the

absolute value of the vector from the center of the Smith Chart to the respective dots. The transmission coefficients can be written as

$$\tau_{\parallel} = |\tau_{\parallel}| \angle \phi_{\parallel} = 1 + \Gamma_{\parallel} \quad (3.1)$$

for the parallel component and

$$\tau_{\perp} = |\tau_{\perp}| \angle \phi_{\perp} = 1 + \Gamma_{\perp} \quad (3.2)$$

for the perpendicular component. Tuning the phase angles of the transmission coefficients,  $\angle \phi_{\parallel}$  and  $\angle \phi_{\perp}$ , is the final task for the meander sheets in order to convert the field from linearly polarized to circular. For a perfectly circular field the phase difference must be 90 degrees. In other words we require that

$$\angle \phi_{\parallel} + \angle \phi_{\perp} = 90 \quad (3.3)$$

Thus each of the two components must experience a phase shift of 45 degrees. By studying the vector geometry of the Smith Chart in Figure 3.1 we can observe that the condition will only be satisfied if the reflection and transmission coefficients have equal amplitudes. Even though the field is perfectly circular, a design with a reflection coefficient of 50 percent will never meet the requirements for a space TLGA. The problem must be addressed and it is simply solved by adding more sheets of meander separated by a distance ( $s$ ) of about a quarter wavelength at the design frequency as illustrated in Figure 3.4. Note that the effective sheet separation will be shifted due to the substrates where the meander pattern is etched. The sheet separation allow us to transform the impedances of the equivalent circuits, i.e. ( $jX_{\parallel}$  and  $jX_{\perp}$ ), for the respective field components to the desired characteristic impedance. Recall that a transmission line will rotate impedances in the Smith Chart. For a three layer configuration, as shown in Figure 3.4, the susceptance of the inner meander lines should be approximately twice the susceptance of the outer layers to reach the center of the Smith Chart.

Determining the geometry of the meander cells for a required susceptance, i.e. the parameters  $d$ ,  $p$  and  $w$  in Figure 3.2, and the line periodicity ( $a$ ) in Figure 3.3 is not a trivial task. A theoretical method is outlined in [31] where T-matrices are used in combination with a methods of moments approach. Furthermore, empirical formulas for the meander susceptances can be found in [32]. A quick engineering solution to the problem of meander geometry is to use initial parameters already derived by well known authors, such as [27], and further re-scale, tune and optimize the values for the problem at hand using modern software tools where e.g. Floquet mode analysis can be used.

## 3.2 Plane to Cylinder Conversion

For the meander plane to cylinder conversion we propose the following method, derived using simple geometric considerations. The number of meander lines on the cylinder can be calculated through

$$N_{lines} = \frac{2\pi R}{k} \quad (3.4)$$

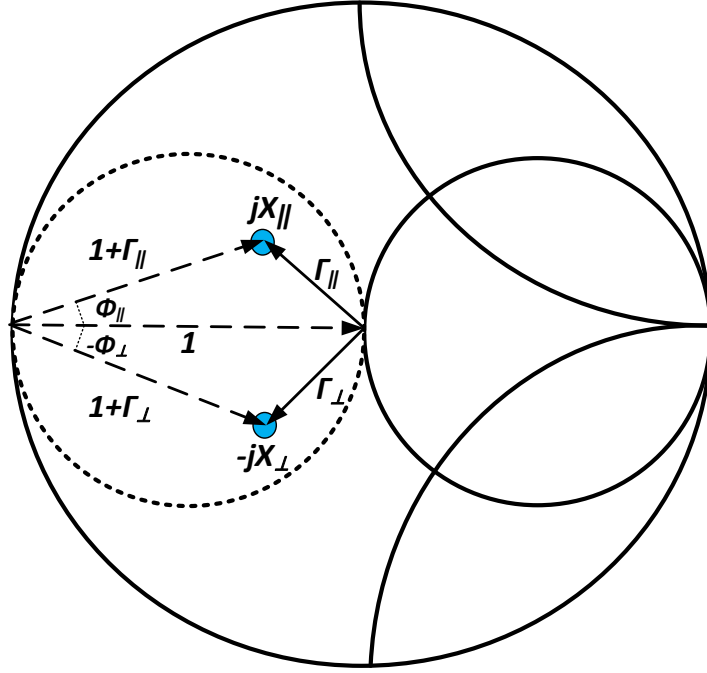


**Figure 3.1:** Single sheet meander design illustration using a Smith Chart.

Where  $R$  is the radius of the cylinder and  $k$  is a 45 degree projection of the distance between the meander lines i.e.

$$k = \frac{a}{\sin(45^\circ)} \quad (3.5)$$

In order to have an even number of meander lines on the cylinder the distance between the lines, i.e. the parameter  $a$  (also shown in Figure 3.3), most likely needs to be tuned if  $N$  is not even. We can express the re-calculation of  $a$ , if required, as

$$a_{cyl} = \frac{2\pi R}{\text{round}(N_{lines})} \sin(45^\circ) \quad (3.6)$$

The expression  $\text{round}(N)$  indicates that the retrieved value of  $N$  from equation 3.4 should be rounded to the nearest integer value. Another equation that can be useful when the layers are wrapped into cylinders are the number of meander cells required for each line, which is simply

$$N_{cells} = \frac{R_s}{p} \quad (3.7)$$

We define the slant length of the meander lines  $R_s$  as

$$R_s = \frac{H}{\sin(45^\circ)} \quad (3.8)$$

Where  $H$  is the height of the cylinder. Note that the cell periodicity,  $p$  in Figure 3.2, may have to be adjusted to avoid discontinuities on the cylinder.

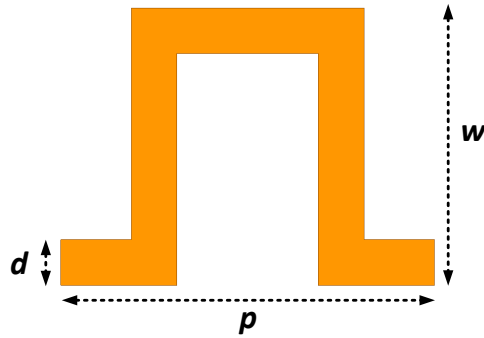


**Figure 3.2:** Design parameters for a meander unit cell. I.e. the cell periodicity ( $p$ ), the cell height ( $w$ ) and width of the meander lines ( $d$ ).

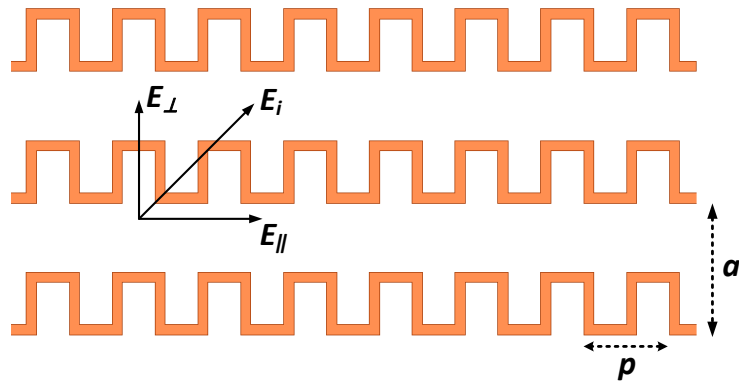


**Figure 3.3:** Illustration of how the incident field should be aligned in relation meander plane for linear to circular polarisation conversion. The cell periodicity ( $p$ ) and the distance between the meander lines ( $a$ ) is also defined.

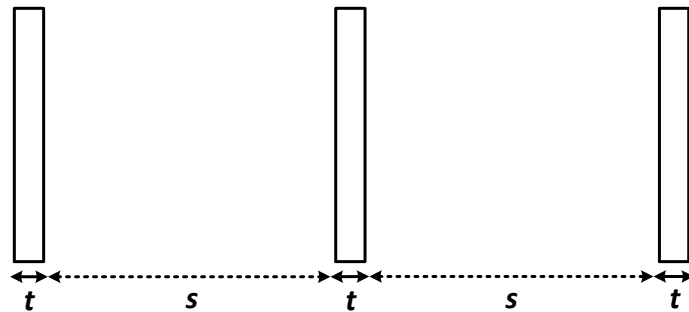


**Figure 3.4:** Parameter illustration for a three layer meander line polarizer. I.e. the substrate thickness,  $t$ , and the spacing between the layers,  $s$ . The spacing between the layers should be around one quarter wavelength at the design frequency.

# 4

## Specifications and Requirements

This chapter will deal with specifications and requirements for the TLGA. The specifications are based on actual data from real space antennas found in e.g. [5] [14] and different internal data sheets at RUAG Space. Since internal data sheets often are classified as intellectual property some specifications have been modified but the general requirements are still applicable. Note that the latter only applies to the mechanical requirements, the presented electrical requirements are valid. The most important mechanical specifications, along with a brief theoretical background, will also be treated. Basic effects that an antenna will experience in space due to the thermal and charge environment is presented in the final section of this chapter. The effects always need to be accounted for prior to a launch. The section about the space environment will be based on theory from [4].

### 4.1 Electromagnetic

The specifications in this section are specific for the biconical horn that is proposed. I.e. a vertically polarized TLGA that, using a meander type polarizer, can be converted to a circularly polarized TLGA. The specifications include the used frequency bands, gain, return loss, side-lobe levels and the requirements specific for the circularly polarized variant i.e. the axial ratio and the cross-polar discrimination.

#### 4.1.1 Frequency and Bandwidth

The commonly used bands for spacecraft TT&C are displayed in Table 1.1. The antenna that is presented in section 6 will be designed to meet the requirements for deep-space  $X_{BAND}$  communication. The design frequencies are 7145 - 7190 MHz for the uplink and 8450 - 8500 MHz for the downlink. The bandwidth is about 50 MHz for both RX and TX. Note that the same antenna element, i.e. a single bicone will be used as both RX and TX antenna. The requirements on the antenna, in terms of bandwidth, will thus be a lot higher. Within the required bandwidth all the individual specifications such as reflection, gain, polarisation and cross-polar discrimination (XPD) must be satisfied.

#### 4.1.2 Gain

The gain is often very application and customer specific and it will strongly depend on specifications of the two WCAs that are used in combination with the TLGA.

Typical elevation coverages for a TLGA include  $\pm 10^\circ$ ,  $\pm 20^\circ$  and  $\pm 30^\circ$  about beam peak. Within the coverage region the gain requirement is greater than -1 dBi but it could be higher depending on the application. We set the requirement to greater than -1 dBi  $\pm 20^\circ$  about the center of beam at  $\theta = 90^\circ$ . Furthermore, the gain slope should be kept below 1 dB per degree in the coverage region.

### 4.1.3 Return Loss

The return loss is defined using the reflection coefficient ( $\Gamma$ ) of the input port to the antenna according to

$$RL(dB) = -20\log(|\Gamma|) \quad (4.1)$$

which should be as low as possible to increase the efficiency of the antenna. We set a requirement of at least 16 dB for the return loss. The fitness function, which will be described in section 5.2.2, will however contain a 4 dB margin.

### 4.1.4 Azimuth Ripple

Azimuth ripple or the variation of the antenna directivity in the horizontal plane should be kept as small as possible. The vertically polarized variant of the biconical horn will have a negligible azimuth ripple since it is a rotationally symmetric structure. The circularly polarized antenna will not be rotationally symmetric due to the finite sized polarizer. The azimuth ripple for the latter antenna should be below 1 dB.

### 4.1.5 Polarisation

The polarisations of the receiving and transmitting antennas are typically either left or right handed circularly polarized on spacecrafts. Often e.g. RHCP is used for the TX Antenna and LHCP for the RX antenna. Vertically or horizontally polarized TT&C antennas are also used in space, the orientation of the satellite and ground station antenna will however become an important factor in this case. The decision of what type of polarisation should be used is thus strongly dependant on the application. For the antenna designs proposed in section 6 we will present one vertically polarized TLGA and one circularly polarized (RHCP) variant.

### 4.1.6 Axial Ratio

Axial ratio is a measure of how circular the polarisation actually is. We define the axial ratio in terms of the RHC and LHC directivity patterns according to

$$AR(dB) = 20\log\left(\frac{|RHC| + |LHC|}{|RHC| - |LHC|}\right) \quad (4.2)$$

An axial ratio of 0 dB corresponds to a perfectly circular polarisation and anything above that can be described as elliptical. If the axial ratio approaches infinity then the polarisation is linear. For a circularly polarized antenna we thus want to keep the axial ratio as low as possible. We set the requirement to less than 4.2 dB within

the specified coverage region of  $\theta = 90 \pm 20$  for the RX band. The requirement on the TX band will be more strict with a level of less than 2.75 dB. These requirements comply with the Juno TLGA presented in [10]. Higher values of axial ratio can also probably be accepted as will be discussed in the following subsection.

#### 4.1.7 Cross-Polar Discrimination

Undesired polarisation components are referred to as the cross-polar components, in some cases however both the co and cross components are desired. The cross-polar component is, for our case, LHCP since we design the antenna to be RHCP. Note that this can be changed by simply changing the tilt angle of the meander lines. The co and cross-polar difference is most commonly denoted as the cross-polar discrimination (XPD) and is defined according to [16]

$$XPD(dB) = 20\log\left(\frac{|RHC|}{|LHC|}\right) \quad (4.3)$$

Where RHC and LHC are two dimensional arrays of the directivity beam patterns for each phi cut. Another useful equation that relates the cross-polar discrimination to the axial ratio is

$$XPD(dB) = 20\log\left(\frac{10^{\frac{AR(dB)}{20}} + 1}{10^{\frac{AR(dB)}{20}} - 1}\right) \quad (4.4)$$

Where AR(dB) is the axial ratio in units of decibels. From the axial ratio requirements the corresponding XPD will be 12.5 and 16 dB respectively for the RX and TX bands. The latest RUAG Space TLGA, dual bicone configuration, as shown in Figure 1.4 and presented in [14], had a requirement of 12 dB XPD. There also exist toroidal antennas, for space, with XPD requirements of 9-10 dB. Thus anything around or above 10 dB can also probably be accepted. In the end, this will depend on the customer requirements where negotiations also play a part.

#### 4.1.8 Side-lobes

The side-lobes of an antenna are in general very undesired and need to be reduced. The goal for the levels was to have side-lobes that are similar to RUAG Space simulated results on TLGAs [14]. Thus, we set the requirement on the far out side-lobe levels of the vertically polarized TLGA to be less than -10 dBi. For the circularly polarized variant the requirement will not be that strict since we introduce non symmetric and other non ideal components. For this case they should be kept lower than -7 dBi. Refer to section 5.2.2 for a more accurate figure of the side lobe specifications for the vertically polarized variant.

## 4.2 Mechanical

The presented mechanical requirements should not be viewed as absolute for the antenna at hand. The idea is only to get an intuitive understanding of what we need to consider in the electrical design for the biconical horn to actually be a viable space

antenna. A viable space antenna must survive the launch and space environment without electrical or mechanical failure. Recall that the mechanical, thermal and electrical aspects of the antenna are equally important for space applications. The same can not be said about a ground based antenna where the requirements are a lot less strict in terms of robustness and thermal characteristics. The specifications described in this section should always be verified through simulations, in softwares such as Ansys Workbench, prior to manufacturing and actual testing on vibration tables. Mechanical simulation results are outside the scope of this thesis but the presented section can be viewed as a reference for future work on the antenna.

The concept of margin of safety and stiffness will be treated in the first subsection of this chapter. The second, third and fourth subsection will treat stationary, random and non-stationary vibrations.

### 4.2.1 Margin of Safety and Stiffness

Margin of Safety (MS) is a commonly used ratio which describes the strength of the designed structure in relation to the requirements. The definition can vary between institutes but the general idea of the ratio can be written as

$$MS = FS - 1 \quad (4.5)$$

Where FS is the Factor of Safety defined as

$$FS = \frac{\sigma_y}{\sigma_w} \quad (4.6)$$

Where  $\sigma_y$  is known as the yield stress and  $\sigma_w$  as the working stress. We could also interpret  $\sigma_y$  and  $\sigma_w$  as the ultimate allowable load and the expected stress respectively. The expected stress is commonly multiplied by a design safety factor. The absolute value of the safety factor is dependent on the condition or device that is studied such as e.g. a yield or ultimate load condition.

Stiffness is another very important figure of merit in the mechanical considerations of a space antenna. All materials have natural frequencies that may be excited if the conditions are right. The natural frequencies, or the modes of the structure, are proportional to both the stiffness and mass. Modal analysis of the antenna is thus very important, where the objective is to reveal at what frequencies mechanical resonances may occur. If a natural frequency, not sufficiently suppressed, is excited in the antenna e.g. during launch it will almost certainly lead to mechanical failure. There is always a requirement on the frequency of the first fundamental mode. The requirement could e.g. be that it must be higher than 160 Hz, i.e. that all resonances below 160 Hz must be suppressed. Modal analysis is a great way to identify the natural frequencies of the structure but to retrieve actual values of the antenna deformation we must excite the structure with a known load, such as a sinusoidal stationary vibration, with respect to a boundary condition.

### 4.2.2 Sinusoidal Stationary Vibration

By exciting the antenna with a sinusoidal stationary vibration a spectrum of deformation versus frequency can be obtained for different parts of the antenna. The spectrum will, of course, peak at the natural frequencies as derived from the modal analysis. Simulation wise, modal analysis can be performed without knowledge of the damping ratio of the structure. To simulate absolute numbers on e.g. Von-Mises stress and deformations of the antenna the damping ratio must be known. The problem is that the damping ratio can only be known through actual measurements of a physical antenna. Previous experience and a general idea of what the damping ratio for e.g. a bolted aluminium structure should be is usually enough in the definition of the damping ratio.

The first row of Table 4.1 displays an example of how specifications could look like for the sinusoidal case. The specifications of row one lists the base accelerations input amplitude for different frequency regions. Note that all values in Table 4.1 are modified. In reality they will be different, with significantly higher amplitudes, for a space antenna but the general principle is valid. The actual values are derived from the conditions on the spacecraft during launch using e.g. accelerometers.

The boundary condition applied in the mechanical simulation software is usually that the antenna is fixed to a large stable structure, as would be the case for a vibrational table or an actual satellite launch. The antenna is furthermore excited by the vibrational load at the fixed supports or through a virtual shaking of the full structure, depending on the software used. Sometimes it is sufficient to estimate the response amplitude ( $A$ ) using the formula

$$A = A_i \sqrt{\frac{1 + 4\zeta^2 \frac{f^2}{f_0^2}}{(1 - \frac{f^2}{f_0^2})^2 + 4\zeta^2 \frac{f^2}{f_0^2}}} \quad (4.7)$$

Where  $A_i$  is the input amplitude of the base acceleration as specified by the first row of Table 4.1,  $f_0$  is the first eigen-frequency of the antenna (which can be derived using modal analysis) and  $f$  is the highest excitation frequency for the studied spectrum area. The damping ratio  $\zeta$  is between 2 - 8 % for a bolted aluminium structure. For the presented TLGA it would be wise to set the damping ratio at about 2% to be on the safe side.

### 4.2.3 Random Response Analysis

Vibrations in a spacecraft, and nature in general, are random. The random vibration analysis can thus be interpreted as a more realistic scenario in comparison to stationary vibration analysis, yet both are important consider. For the random response analysis we study the response at a set of weak nodes in the antenna structure, e.g. regions where two objects intersect such as bolted connections. We can also visualise the random response as Von-Mises stress for the full structure in order to find weak regions.

A specification example of the amplitude of the input random acceleration spectral density is displayed in the second row in Table 4.1. Note that the analysis must be performed on all degrees of freedom in the system, in a cartesian system it would correspond to responses in both x, y and z directions. The results of a random response analysis can only be expressed in terms of a probability within some sigma level. In other words we can never state the results of the random response analysis are 100 % correct. But we may state they have a 99.73 % probability if e.g. a three sigma level is used.

#### 4.2.4 Non-stationary Vibration

Non stationary vibration, also known as shock, is another important mechanical figure of merit to consider. The principle is simply to study the response of the structure if it experiences a sudden change in its state of rest. Refer to row three in Table 4.1 for example values of a non-stationary vibrational input.

**Table 4.1:** Specification example for vibration analysis. Vibration analysis should be performed prior to all launches of a spacecraft system. Note that the actual values will be different for a space antenna with e.g. significantly higher amplitudes. The values are only supposed to act as an illustration for the type of analysis the mechanical engineer will work with in a space antenna designs.

|                                      |                             |
|--------------------------------------|-----------------------------|
| Stationary vibration, sinusoidal     | 8 mm @ 2 - 20 Hz            |
|                                      | 25 $m/s^2$ @ 20 - 250 Hz    |
|                                      | 50 $m/s^2$ @ 250 - 600 Hz   |
| Random acceleration spectral density | 4 $m^2/s^3$ @ 5 - 300 Hz    |
|                                      | 2 $m^2/s^3$ @ 300 - 2000 Hz |
| Non-stationary vibration incl. shock | 400 $m/s^2$ during 12 ms    |
|                                      | 1200 $m/s^2$ during 7 ms    |

### 4.3 The Space Environment

Space is not as empty as the name suggests. Radiation from the sun, planetary albedo, gravity gradients, magnetic fields, particles from outer space and even artificial debris will affect the performance of the antenna. In order to design an antenna that can be used in space all of these effects need to be accounted for. We will discuss, on a simplified and fundamental level, three very important effects in the following subsections.

#### 4.3.1 Multipaction

Multiple impaction, or multipaction, can be described as an avalanche type of effect that can occur between two conductors if the RF fields are sufficiently strong. The effect is triggered by a discharge and further enhanced by secondary emissions from colliding electrons in the electrodes. Multipaction effects can lead to both electrical

and mechanical failure. Apart from the applied RF power it will also depend on the vacuum condition, geometry, frequency and potential material contaminations which can enhance the effect. The latter statement is one of the reasons why space antennas must be handled with care in clean rooms. Multipactor breakdown analysis will not further be treated in this thesis but simulation wise it can be performed with conventional EM analysis tools such as CST Studio Suite. The results of these simulations can for example put a restraint on how much power the antenna can handle. Multipaction analysis can also be performed using other software tool-kits such as the European Space Agency Multipactor Calculator [34]. However it has limited functionality and can, for example, not simulate actual breakdown powers of an antenna but for a set of predefined materials.

### 4.3.2 Outgassing

Outgassing is simply another word for the release of gas that was trapped, for example in small pockets, in the material during e.g. manufacturing. For an antenna in vacuum the sudden escape of gas can lead to the release of volatile mass particles that can damage the antenna and even other parts of the satellite. The outgassing requirements on a material are set by the space agencies responsible for the spacecraft launch. In the material selection of the antenna it is thus important to only consider those that have been approved. A database of materials that meets outgassing requirements, according to NASA standards, can be found in [33]. Only approved materials will be used for the presented TLGA. However, it is not sufficient to simply select approved materials. Actual testing, in a vacuum chamber, must be performed prior to the delivery of the space antenna.

### 4.3.3 Thermal Analysis

In thermal analysis there are basically three worst case scenarios that need to be considered that can deform, or severely damage the antenna. Firstly, the hot case, where perpendicular radiation from the sun is incident on the surface. Secondly the cold case with minimum radiation from the sun and albedo from the earth. The hot and cold temperatures will depend on the mission, for a terrestrial satellite typical values ranges from -150 to 150 degrees celsius. Temperature gradients also need to be considered i.e. where one side of the antenna is extremely hot and another cold.

Thermo-elastic calculations can be performed using finite element method softwares such as Ansys Workbench or by hand through e.g. thermal balance equations. The latter method will become too complex for a full antenna structure so in almost all cases finite element methods are used. Manufactured space antennas are also always tested in thermal chambers for the worst case scenarios. Thermo-elastic deformations will be considered in the design of the biconical horn by employing a capacitively coupled coaxial feed to the upper cone. This will allow the center conductor to float in relation to the cones to account for thermal mismatches in the materials comprising the antenna. The latter will be further discussed in Chapters 6 and 7.



# 5

## Design Methods

### 5.1 Electromagnetic Modelling

The electrical modelling of an antenna is one of the most crucial aspects in the design, especially if theory is not able to accurately predict the behaviour of the antenna. A theoretical foundation for the model is of course very important. For the considered antenna refer to chapters three and four. There are many different software tool-kits where experimental work and modelling of an antenna can be performed. The two most common full wave packages are CST Studio Suite and Ansys HFSS [35] where the latter will be used in this thesis.

Matlab is another important tool, both for antenna calculations but also the modelling initiation and post-processing of e.g. exported far field data [36]. An extensive system simulator was developed using Matlab in combination with HFSS. The developed software was used to quickly configure, solve and analyze different biconical antennas and profiles in an automatic fashion. In this way many different antenna configurations and setups were investigated in a relatively short period of time. Matlab can also, with great benefit, be used in an optimization procedure. The developed optimization software will be extensively described in section 5.2.

### 5.2 Optimization

Optimization is something that is always performed after a good initial design is obtained, hence the word optimization. In the end optimization is about finding the minimum of a function, we may of course also formulate it as a maximisation problem. Many different methods for solving maximisation problems have been proposed throughout the years [37]. The most straight forward way, for a simple function, is just to calculate its derivative. But the function, or problem, may have an infinite amount of solutions that are in close proximity. Using simple methods such as derivatives and Newtons method works for many problems, but as soon as the function becomes too complex we have to look for other methods. An example of a complex function is an antenna with a large amount of parameters defining the geometry and thus the characteristics. Using biologically inspired algorithms is a common way to minimise complex functions. We will denote the complex functions for the antennas as fitness functions. Note that the problems will be formulated as minimisation problems, i.e. a smaller fitness value is equivalent to a better antenna in comparison to a high fitness.

### 5.2.1 Biologically Inspired Algorithms

Flock behaviour has intrigued scientists for a very long time. Early models of flock behaviour, fish schools and other organisms were presented in the 80:s with the purpose of simulating social behaviour. It was not until recently, on the historical scale of antennas, that the swarming behaviours of bird flocks were actually used in computer programs in order to perform optimization [38]. Let us for convenience and generalization change the name bird to particle.

The very basic principle of particle swarm optimization is simply that a swarm of particles will find an optimal point, or a set of points, much faster than a single particle. In the swarm, each particle is aware of its own best local solution as well as the swarms global best solution, hence the uniform motion. If the goal for the particles is to find the best solution it will consequently swarm towards it. In an analogy with antennas, we can describe to the particles, using fitness functions, how we would like our antenna to behave. The problem is that it most likely exists an infinite amount of solutions that can be in very close proximity if the parameter space is large. If the conditions are properly set the swarm will find good solutions, perhaps not the best, but hopefully more than sufficient for the requirements.

Particle swarm optimization is closely related to another commonly used biological algorithm, i.e. the genetic. Instead of using the optimizing behaviour of swarms we make use of the Darwinian principle of evolution. Evolution is another way of saying that nature performs optimization, recall Darwin's finches and how the form of their beaks were optimized over time due to the different conditions on the Islands of Galápagos. The interested reader can refer to [37] for more details on evolutionary programming.

### 5.2.2 Fitness Evaluation

Several fitness functions, or cost functions, were developed in order to handle the strict specifications of a TLGA in space. More explicitly the cost functions focused on bandwidth, gain, side-lobes and return loss using different weights in the combination process. We will not outline the full details of the fitness functions but we will review the basics. The cost function for the return loss is defined in quite simple terms according to the conditional statement

```
if  $S_{11,i} < -20$  then  
|  $S_{11,Fitness} = 0$   
else  
|  $S_{11,Fitness} = S_{11,i} + 20$ 
```

where the subscript,  $i$ , is an indication that the algorithm should be applied to all frequencies that are considered in the design. The fitness function for the return loss, where all values are in decibels, will thus acquire the value zero if the goal of 20 dB is reached. The gain, beam width and side-lobe fitness requirements are illustrated in Figure 5.1. The figure displays an example for the elevation beam

pattern of an antenna. For the main beam ( $\theta = 90 \pm 20deg.$ ) we required that the gain should be greater than -1 dBi. By including a margin of 1 dB in the fitness function we define the cost of the main beam as

```

if  $all(E_{Theta,Dir}(70 : 110)) > 0$  then
  |  $MainLobe_{Fitness} = 0$ 
else
  |  $MainLobe_{Fitness} = 0 - min(E_{Theta,Dir}(70 : 110))$ 

```

i.e. if the directivity at every elevation angle from 70 to 110 degrees satisfy the condition of being greater than 0 dB then the cost is set to zero. If the goal is not satisfied, the fitness function for the main beam will acquire a value that is the difference between the gain specification and the minimum directivity in the main beam. The fitness functions for the side lobes are defined in a similar way but with other signs. We divide the side lobe cost functions in two areas from 0 to 25 degrees, where it is required to be lower than -10 dB, and from 25 to 50 degrees where the requirement is less strict i.e. -5 dB. Due to the symmetry of the E-plane pattern we may also consider the pattern as one sided, i.e. mirrored in the  $\theta = 90deg.$  plane. In terms of conditional statements we may express it as

```

if  $all(E_{Theta,Dir}(0 : 25)) < -10$  then
  |  $SideLobe(Area1)_{Fitness} = 0$ 
else
  |  $SideLobe(Area1)_{Fitness} = max(E_{Theta,Dir}(0 : 25)) + 10$ 

```

and

```

if  $all(E_{Theta,Dir}(25 : 50)) < -5$  then
  |  $SideLobe(Area2)_{Fitness} = 0$ 
else
  |  $SideLobe2(Area2)_{Fitness} = max(E_{Theta,Dir}(25 : 50)) + 5$ 

```

In summary, all fitness functions are defined in terms of minimization problems and will always be positive. If all specifications, including margins, are satisfied the cost functions will be zero i.e. the best possible antenna in an optimization run is defined to have a fitness of zero. Each of the functions also needs to be combined into a single cost function. How each individual function should be weighted in relation to each other is not a trivial problem. E.g. if side lobes are of greater importance than the gain of the main beam they should have a higher weight, or importance, in the cost definition. Trial and error, as well as having actual data on the far fields and S-parameters of an antenna that requires optimization, is a good approach to obtain a correct cost weighting and thus defining the total fitness function.

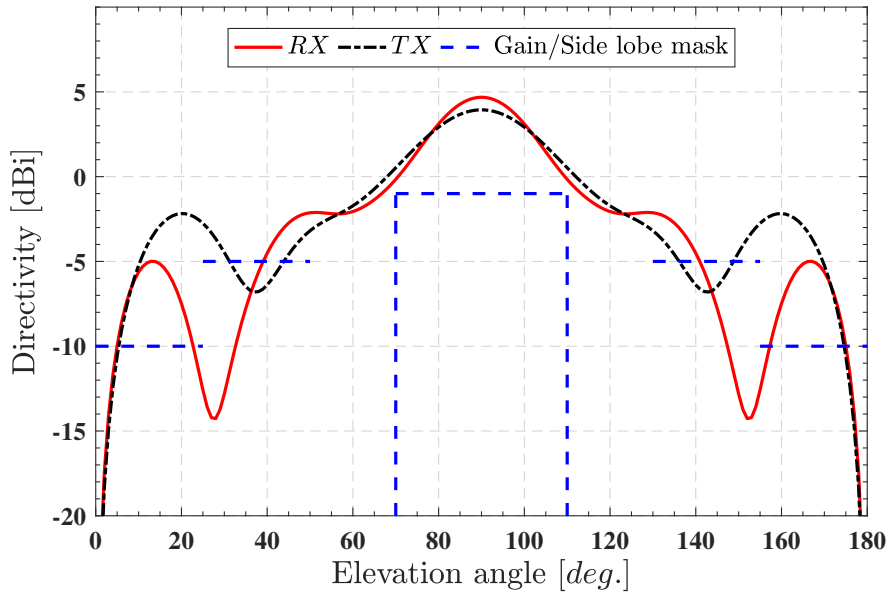


**Figure 5.1:** Illustration of the fitness functions for the main beam and side-lobes. We require a gain greater than - 1 dBi for the main beam and lower than -5 dBi and -10 dBi respectively for the side lobe areas that are displayed in the figure.

### 5.2.3 Spline-defined profile

The optimization procedure via a spline-profile is a relatively new method introduced in the 21th century and it has, until now, only been applied in the design of state-of-the-art feed-horns [24] [39] [40]. The numerical profile used for the biconical antenna design is illustrated in Figure 5.2. Only symmetric bicones are considered and the profile, in the illustration, is thus fully defined by seven interpolated points. The seven point definition excludes the initial starting point of profile which is set to a constant value defining the gap size and diameter, i.e.  $G$  and  $D$  in Figure 2.1.

A key benefit in defining the profile as a set of interpolated numerical points is the possibilities it presents to a stochastic optimization algorithm. By allowing a freedom in both  $x$  and  $y$  for each of the individual points, refer to Figure 5.2, we open the possibility to find an infinite amount of profile options that are hard or even impossible to describe analytically. The fitness function, as presented in section 5.2.2, is our way to present information to the optimization algorithm on what type of specifications the antenna should fulfil. We have no idea how the geometry of the profile will be defined, should the algorithm converge to the optimal design, but there are ways to keep the convergence under control. Chartering the unknown and opening for the possibility of finding new high performing horn profiles is what makes stochastic optimization a very interesting method. Especially when it is applied to new areas, such as in this case, to the biconical antenna.

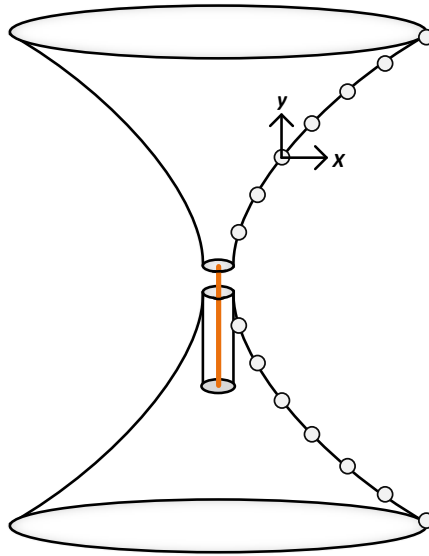


**Figure 5.2:** Illustration of a numerically defined profile for the biconical horn. The profile is defined by seven points, excluding the start value of the profile defining the gap size and diameter. Only symmetric bicones are considered and as such the points are mirrored and extruded in  $y$

Some things that are very important to consider and control in the numerical profile optimisation are

- Which parts of the profile that should be focused on and what effect this will have on the radiation pattern and e.g. input impedance of the biconical horn. E.g. the side-lobes are mainly determined by the taper, i.e. the end points of the profile. Thus, it is probably good to focus the optimization on that part if side-lobe levels are of main concern. Vice-versa, the input impedance of the antenna is greatly affected by the inner radius ( $D$ ) and the gap size ( $G$ ) as defined in Figure 2.1. For matching purposes, it is thus a good idea to focus on the first points of the profile. Combining all the specifications into a single fitness function and optimizing the full profile may thus not be an optimal approach.
- The number of points in the profile. A smooth profile requires a certain amount of points, which in most cases can be based on a fractional number of the wavelength used. In numerical profile optimization a trade-off has to be made. Too many points may lead to problems regarding the convergence of the optimization process and thus also the optimization time. Too few points can affect the radiations characteristics very negatively since the profile is no longer smooth. The number of points required to make a smooth profile can be significantly reduced by using basic Matlab techniques combined with tools in EM-simulation software. Yet, more points may still be required to find an antenna that meets

the fitness goals. Exactly how this should be done can not be said since it depends on the setup and e.g. the size of the antenna. Often trial and error is a good approach as well as having a reference antenna with a very large number of points.

- The simulation time. A rotationally symmetric EM-simulation tool, such as AKBOR, can be very beneficial for the initial optimization process due to its speed. However problems arise at a later stage in the antenna design if non-symmetric components are introduced. The rotationally symmetric softwares are then no longer applicable. The techniques, for e.g. reducing the number of optimization points, becomes crucial due to the increased simulation time in full wave finite element method softwares such as Ansys HFSS.
- The maximum and minimum values for the numerical points in the stochastic algorithm. If we let the the points have a freedom of e.g. ten percent in two dimensional space it might be hard to reach convergence within a reasonable time period. Reducing the search space is the most common solution, in some cases a large search space is, however, required and fitness convergence could take several months depending on the setup. Another approach could be to use a large freedom in the initial stage to find interesting designs, then proceed to refocus the algorithm on these points with a smaller freedom. This might not be an optimal approach but it can save a lot of time and still allow for very high performing antennas.

All of these points needs to be carefully considered and analyzed in order for the design to be successful. Using luck, i.e. combining all points into a single entity, such as both reflection and far field goals, as a design approach in numerical stochastic optimization may work but it is not good practice. Furthermore, it wont allow us to control if e.g. the profile will be mechanically viable. It will also most likely take a very long time to converge and even if it does, the converged design may still not be the optimal for the antenna at hand. It is, of course, very important that the antenna that is optimized has a good foundation. In our case a profile that looks promising both for the far fields as well as for the matching criteria.

### 5.2.4 Optimization System Routine

Optimization of antennas can solely be performed using functions in HFSS. This may be suitable for fast optimization routines of e.g. the reflection coefficient. For our case it is important that we have control of both the optimization algorithm and the definition of the fitness functions. We also require a way to reconfigure the profile based on the results from the the postprocess data of the simulated antenna and the stochastic algorithm. Using the built in functions of HFSS is thus not sufficient and we need to look for other methods. HFSS is a very versatile program and it provides a way to control and write functions to the modelling software through Visual Basic for Applications (VBA). The VBA scripting language is very straight forward and the basic functions can quickly be learned without prior programming

experience. HFSS also provides the means to record to VBA, i.e. producing a script that contains the code for e.g. an antenna that was designed graphically. Using the described approach we can quickly learn how an antenna can be configured and analyzed using VBA scripting language in HFSS.

The optimization procedure is displayed in Figure 5.3. The bicone is designed graphically in HFSS using a parametric approach for each component of the antenna. The other way, as described, would be to build the antenna entirely using text based commands. We found it more convenient to design the antenna graphically. Each element of the antenna can still be controlled using scripting since it is parameterized, another advantage with the latter approach is that the VBA code will be more compact. The initial parameterized values of the antenna, e.g. a sinusoidal profile and other information such impedance of the feeding transmission line, are generated and set in Matlab. Using Matlab, we proceed to generate VBA scripts that updates the antenna parameters in HFSS. Note that the program also needs to start the software and upload the script. If CST Studio Suite was to be used it is possible to have the EM-software as a session handle in Matlab and upload the script during run-time. Unfortunately this is not possible with HFSS, but in the end the restart delay of the software will be small compared to the simulation time. We also recommend to turn off the graphics in HFSS when an automatic session with Matlab is initiated to speed up the process. When the parameters of the antenna are updated the control program continues with solving the geometry. The VBA script is finalized by exporting the far fields and S-Parameters back to Matlab. Post-processing of the far field data includes directivity normalization and e.g. the conversion to Ludwigs third definition. The stochastic algorithm evaluates the fitness of the antenna, as described in section 5.2.2, and generates the new parameter values. This is performed iteratively by the algorithm until a final converged solution is obtained.

### 5.3 Mechanical Design

The mechanical design of an antenna is commonly performed in a dedicated CAD software for mechanics such as Ansys Workbench [35]. The mechanical part of the antenna includes e.g. bolts, fixtures and the mounting of the meander layers. The actual mechanical design and the simulations are outside of the scope of this thesis but it must always be considered and thought for in the electromagnetic design. Recall that some mechanical theory and requirements are discussed in section 4.

Mechanically, there are quite a few things the EM-antenna designer needs to consider. One very crucial part, in this aspect, for the TEM excited bicone antenna is the coaxial center conductor that feeds the upper cone. If the antenna is not properly stabilized the center conductor will deform, or even crack, during the launch of the spacecraft. A deformed, coaxially fed, biconical horn is illustrated in Figure 5.5. The shown deformation was due to a modal eigen-frequency that was excited in the structure at a frequency of 67 Hz.

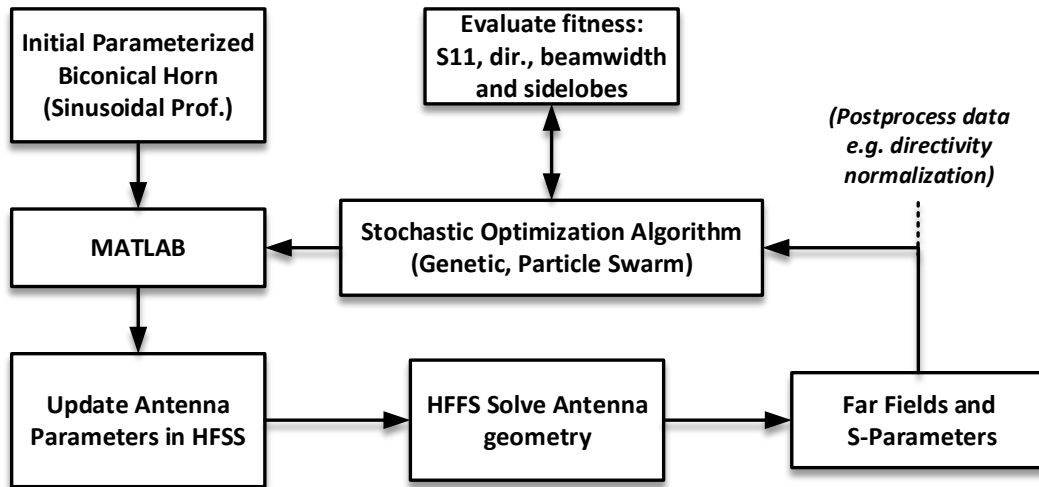


**Figure 5.3:** Block diagram of the optimization procedure using Matlab and VBA Scripting in combination with the EM-Modelling tool Ansys HFSS.

We must consider ways to suppress the mechanical resonances in order to have a coaxial feed that is stable. This will be solved by the polarizer, which apart from converting the field to RHCP, also provides the mechanical stability. The simulation results from the mechanical requirements discussed in section 4.2 is thus very important in the continued design of the antenna. For example it might be found that thicknesses of the meander layers of the design are not enough to suppress the eigen-frequencies of the structure, or rather keep the response within the specifications. In such a scenario the thicknesses of the meander layers may have to be increased. Most likely this will not be the case since we will keep this in mind in the design of the layers by using a very robust fibreglass substrate (FR4).

If the electrical properties of the antenna are within specifications, with a good margin, the mechanical design may be initiated. A simplified design flow chart, for a space antenna, is illustrated in Figure 5.4. The EM optimized antenna is often simplified, in order to render fast simulations, using e.g. ideal feeding, infinitely small perfect sheets and other ideal components. A more realistic model, with realistic feeding and thickness of e.g. copper and aluminium sheets to introduce losses is a good first step to verify the antenna characteristics. Once satisfactory results are achieved the model is exported (.sat is a common data format) to a mechanical cad tool, such as Ansys Mechanical. We then proceed to iterate between the EM analysis tool and the mechanical cad tool in order to find a design that meets all the fitness criteria. Sometimes, the antenna designer also simulates the antenna on the complete satellite model to check spacecraft scattering, interference regions and to make sure there is a 360 degree radiation coverage around the satellite [5]. In many cases, this part is left out or performed by the customer and the spacecraft system designer. The element characteristics are often sufficient figure of merits for an electrical antenna designer.

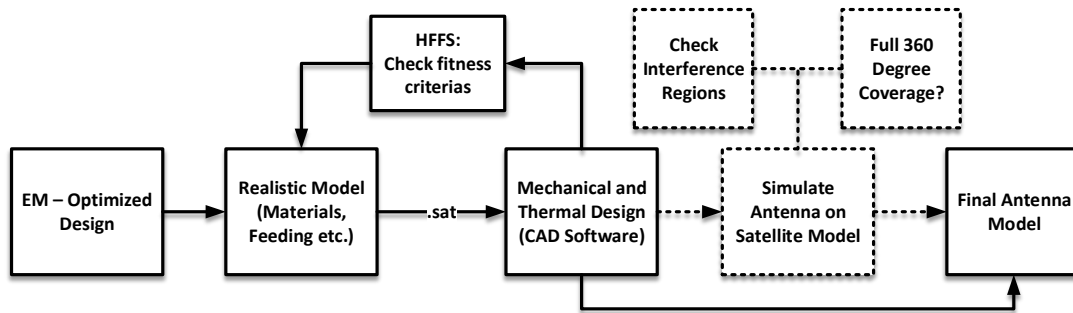


**Figure 5.4:** Block diagram of a typical mechanical design procedure for a space antenna. The antenna simulation on a complete satellite is often left out and the antenna element characteristics are considered sufficient.

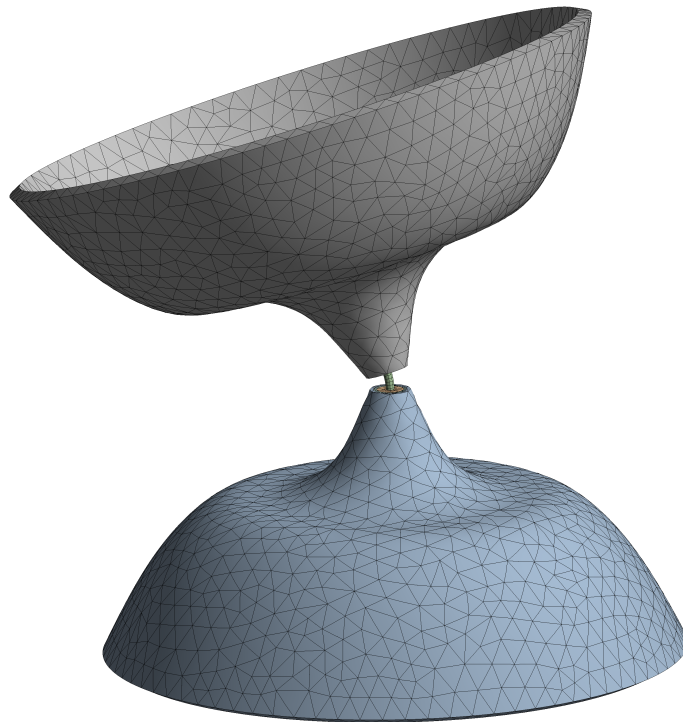


**Figure 5.5:** Illustration of a deformed TEM excited biconical horn. The deformation or even total mechanical failure, i.e. that the center conductor is breached, will occur during the launch of the spacecraft if not properly stabilized by an external structure. For a ground based application the center conductor will not deform unless heavily stressed.



# 6

## Results

### 6.1 Selection of Biconical Horn Profile

This section is introduced with directivity design curves for different profiles. The results are compared in relation to a standard straight profile bicone. Furthermore, beam patterns will be investigated with the goal of finding a profile that can be used as a base for spline-defined optimization. The intention is to find an antenna with good characteristics that can operate in duplex with only one antenna element for both RX and TX. The presented curves can, of course, also be used for other design purposes.

#### 6.1.1 Directivity Design Curves

In section 2.1 the theoretical design for a straight profile is outlined where, among other things, directivity design curves are derived using equation 2.1. To derive analytical expressions for other profile options is far from straight forward. Through the simulation routine, discussed in section 5, the situation can be simplified if the proper software algorithms and modelling techniques are imposed.

Figure 6.1 displays two different situations, in the upper plot the cone radius is one wavelength whereas in the lower the radius is two wavelengths. For the two cases the aperture height is swept and the directivity at the beam center is logged. The sweeps could, of course, be performed for other cone radii but the two presented cases were found sufficient for the requirements at hand. Deriving contour plots, as shown in Figure 2.3 for the straight profile, could also be beneficial. The contour plot derivation was found to be too time consuming, simulation wise, due to the large grid sweeps that are required.

The profiles behave as expected, with the same reasoning as outlined in section 2.1, i.e. that an optimal antenna geometry exists for each case. Each profile exhibits different characteristic and we can clearly see benefits, such as the possibility of size reduction while still maintaining the directivity performance. A more clear illustration of one interesting case is displayed in Figure 6.3. In the figure two curves are compared, one from the upper plot in Figure 6.1 and one from the lower, i.e. their radii are separated by one wavelength. The interesting result with respect to Figure 6.3 is the benefits a sinusoidal profile provides. More explicitly we see that by profiling the bicone with a sinusoidal function we can decrease the aperture height by 0.4 wavelengths.

In addition we can reduce the cone radius with a factor of two in comparison to a straight profile bicone while maintaining about the same directivity. Possibly, the sinusoidal profile would be a better option for the Juno Spacecraft TLGA presented in [10]. However, if we study the lower plot of Figure 6.1 we see that the parabola and the sinusoid, of order two, are in close proximity with respect to geometry and directivity. The large benefits of the sinusoidal profile seems thus to be for lower cone radii in comparison to the parabolic shape.

### 6.1.2 Beam Patterns of Analytical Profiles

By selecting the optimal antenna geometry for each case displayed in the upper plot of Figure 6.1 we can study the characteristics of the radiation patterns. The design frequency is the geometric mean of the upper and lower bound of the RX and TX band respectively. Each of the six simulated geometries are shown in Figure 6.2. The elevation patterns of the cases are presented in Figure 6.4. The red curves are the beams at the center of the transmitting band, i.e. 8475.0 MHz, and correspondingly for the receiving band in black at 7167.5 MHz. The gain mask in blue can be viewed as a reference for how well the patterns are within the main beam requirements which is defined in section 4.

Of the displayed patterns only the second order sinusoidal profile shows promise and is within the main beam requirements. Other profiles, such as the common straight bicone, exhibit characteristics with insufficient promise for a further evaluation. The latter statement includes the requirements for the side-lobes levels outlined in section 4.1.8. The sinusoid ( $p=2$ ,  $A=1$ ) is selected as a base for the continued design of the dual band biconical horn.



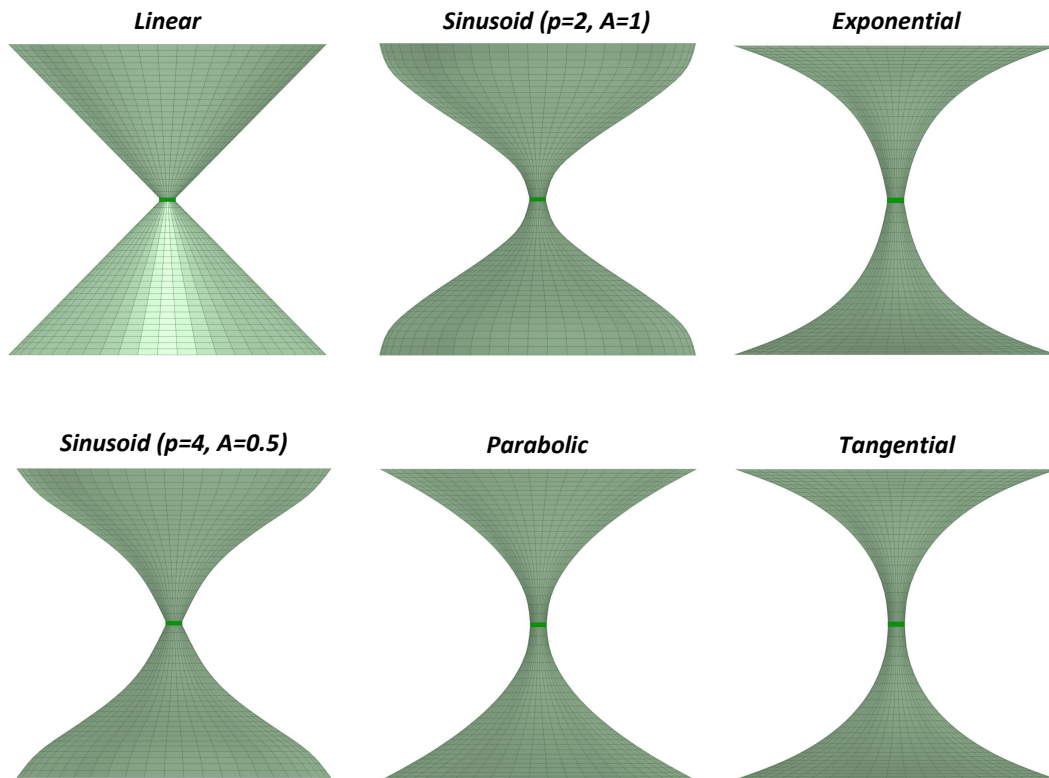


**Figure 6.2:** Geometric illustration of the profiles that were investigated. I.e. the linear, exponential, parabolic, tangential and two variants of the sinusoidal profile of different order ( $p$ ) and linear taper ( $A$ ). The corresponding elevation patterns are displayed in Figure 6.4.

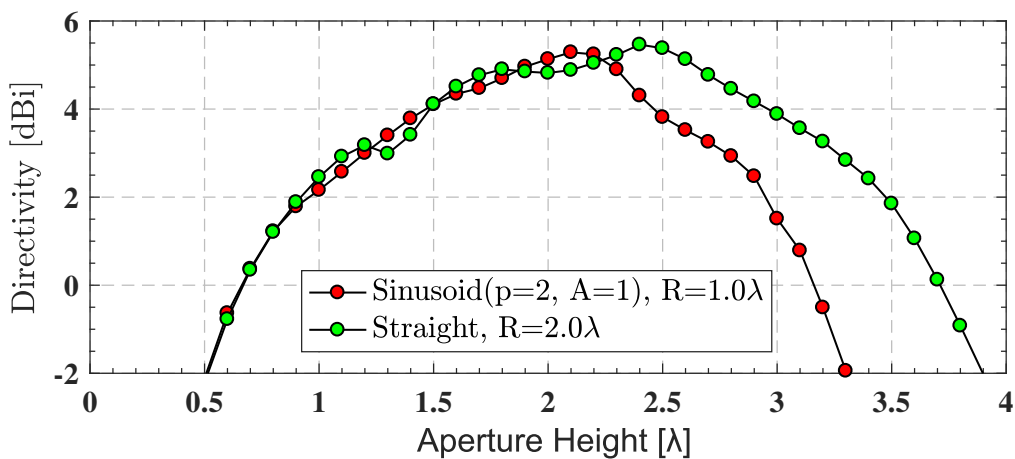


**Figure 6.3:** Comparison of directivity versus aperture height for the sinusoidal and the straight profile respectively. Note that the curve for sinusoidal profile is derived using a cone radius of one wavelength whereas the straight profile has a radius of two wavelengths.

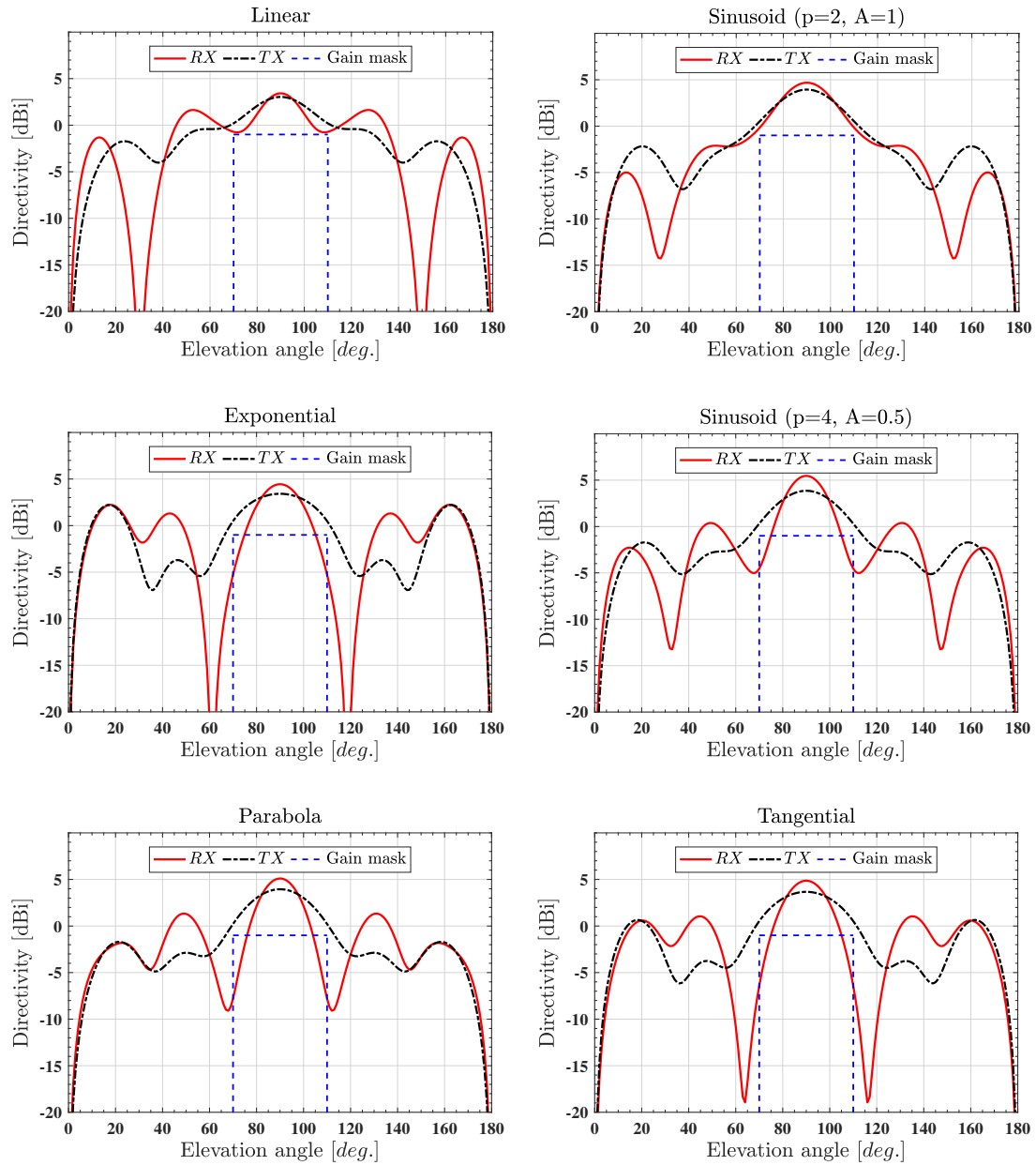


**Figure 6.4:** Radiation patterns for the studied profiles. The red curves indicate the pattern at the center of the TX band and black curve the center of the RX band i.e. 8475.0 and 7167.5 MHz respectively. The gain mask is indicated in dotted blue.

## 6.2 Dual Band Vertically Polarized TLGA

The radiation pattern characteristics of the second order sinusoid in Figure 6.4 is within the gain requirements listed in section 4.1. The side-lobes, however, still require suppression to a lower level. We propose to use the method of spline-defined optimization outlined in section 5.2 to shape the profile in order to meet the required characteristics. I.e. we require a clear directivity margin for the main beam, suppressed side-lobes and good return loss at both bands.

### 6.2.1 Spline-defined Profile Optimization

The performed spline optimization used a seven point definition, the sinusoidal profile was used as base for the initial parameter space. It was optimized with a large freedom for the spline parameters in the first stage. The optimization algorithm was furthermore refocused with a smaller freedom on the best result from the initial stage. The approach was found to be very effective. Prior to the algorithm refocusing the horn was defined by the points listed as nominal values in Table 6.1. The lower and upper bound for the optimization was  $\pm 5\%$  respectively of the nominal value. The start values of the profile, denoted as  $HP\_XMIN$  and  $HP\_ZMIN$  in Table 6.1, are fixed and not optimized. Note that they correspond to  $\frac{D}{2}$  and  $\frac{G}{2}$  respectively in Figure 2.1. The results of the optimization run is displayed in Figure 6.5. After about one week of iterations, or the simulation of 3500 different profiles, we can observe a clear convergence with improving fitness. Running the optimization slightly longer could possibly have been beneficial but the results were found satisfactory. The resulting profile and geometry of the horn is illustrated in Figure 6.6. The final aperture height is 85 mm and the antenna diameter is 90 mm.

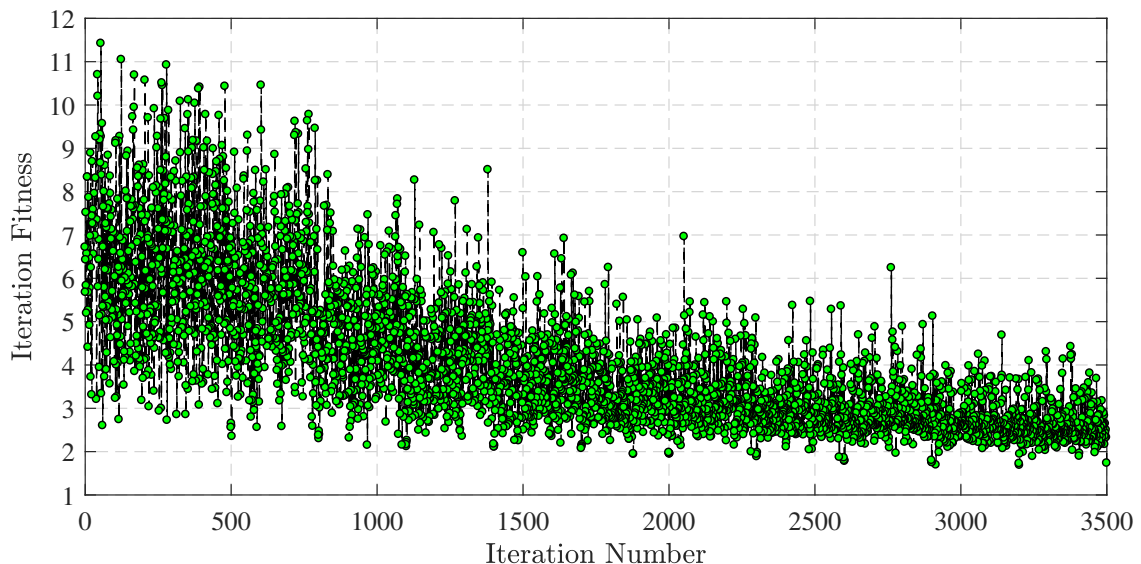


**Figure 6.5:** Iteration fitness for an optimization run on the X-Band TLGA. The algorithm is focusing on the horn profile using a total of 14 geometry parameters.

**Table 6.1:** Profile coordinates of the biconical horn for the optimization run displayed in Figure 6.5. The nominal value corresponds to the initial profile, the upper and lower values are the maximum and minimum values that are allowed in the optimization process. In this case the numerical points of the profile have a freedom of 5 percent. The profile coordinates are illustrated in Figure 2.1 where we now define a global Cartesian coordinate system that is located in the center between the upper and lower cone. Note that the minimum values  $HP\_XMIN$  and  $HP\_ZMIN$ , corresponding to  $\frac{D}{2}$  and  $\frac{G}{2}$  respectively in Figure 2.1, are fixed and not optimized.

| <i>Profile Coord.</i> | <i>Lower [mm]</i> | <i>Nominal Value [mm]</i> | <i>Upper [mm]</i> |
|-----------------------|-------------------|---------------------------|-------------------|
| <i>HP_XMIN</i>        | 1                 | 1                         | 1                 |
| <i>HP_X2</i>          | 2.69              | 2.83                      | 2.97              |
| <i>HP_X3</i>          | 7.03              | 7.40                      | 7.77              |
| <i>HP_X4</i>          | 16.09             | 16.94                     | 17.79             |
| <i>HP_X5</i>          | 22.46             | 23.64                     | 24.82             |
| <i>HP_X6</i>          | 27.72             | 29.18                     | 30.64             |
| <i>HP_X7</i>          | 34.37             | 36.18                     | 37.98             |
| <i>HP_XMAX</i>        | 40.88             | 43.03                     | 45.18             |
| <i>HP_ZMIN</i>        | 0.50              | 0.50                      | 0.50              |
| <i>HP_Z2</i>          | 5.20              | 5.48                      | 5.75              |
| <i>HP_Z3</i>          | 12.58             | 13.24                     | 13.90             |
| <i>HP_Z4</i>          | 17.05             | 17.95                     | 18.85             |
| <i>HP_Z5</i>          | 17.79             | 18.73                     | 19.66             |
| <i>HP_Z6</i>          | 22.54             | 23.73                     | 24.91             |
| <i>HP_Z7</i>          | 29.43             | 30.98                     | 32.53             |
| <i>HP_ZMAX</i>        | 42.42             | 44.66                     | 46.89             |

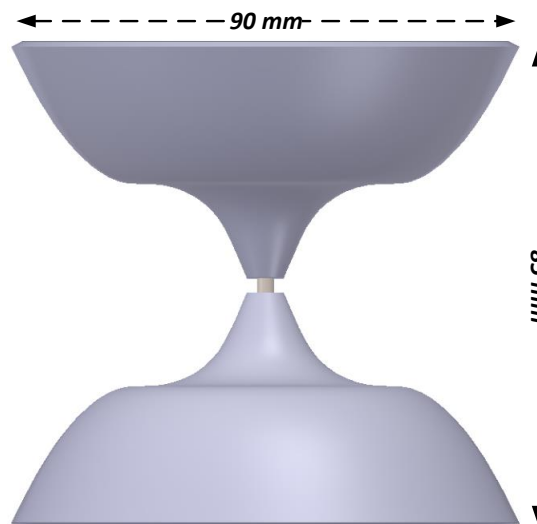


**Figure 6.6:** Geometry and profile illustration of the proposed vertically polarized biconical horn. The profile is derived using a stochastic algorithm applied on the spline points of the horn.

### 6.2.2 Elevation Beam Pattern

The radiation pattern, in  $\theta$ , of the optimized vertically polarized antenna is displayed in Figure 6.7. The azimuthal variation of the antenna is not shown since it is negligible, and the phi cuts have been averaged. The 1 dB deviation in side lobe level on each side of the beam, for the lower frequencies, are due to a small effect from the coaxial feed. This was concluded by studying the radiation pattern of the antenna using an ideal feed as excitation, i.e. a lumped port, and observing the difference when the coaxial connector was introduced. For the higher frequencies the effect from the feed is negligible, which can be used as another step in the validation of the hypothesis that the effect is from the feed.

Comparing the elevation pattern of the original sinusoidal profile in Figure 6.4 with the spline-optimized horn, in Figure 6.7, we observe a significant improvement. The side lobes are suppressed to about -9.5 dBi for the TX band and -13 dBi for the RX band. Furthermore, there exists a 2-3 dB margin at the edge of the coverage region in relation to the requirement of -1 dBi as indicated by the gain mask in Figure 6.7.

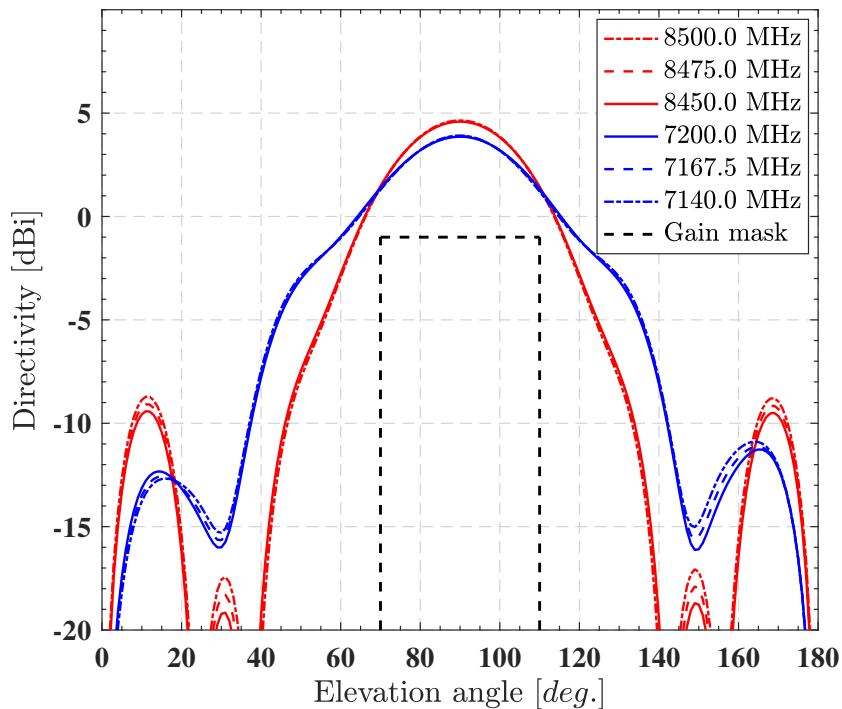


**Figure 6.7:** Radiation pattern, in  $\theta$ , for the vertically polarized spline-optimized biconical horn. The red curves display the lower, upper and center frequency of the TX band and equivalently for RX band in blue. The gain mask is indicated in dotted black.

### 6.2.3 Return Loss

The simulated reflection coefficient for the antenna is displayed in Figure 6.8. By further tuning the gap size and diameter,  $G$  and  $D$  in Figure 2.1, a reflection lower than -18 dB was obtained for both bands. The reflection coefficient could be improved by further optimizing the variables  $G$  and  $D$  but -18 dB were found sufficient.

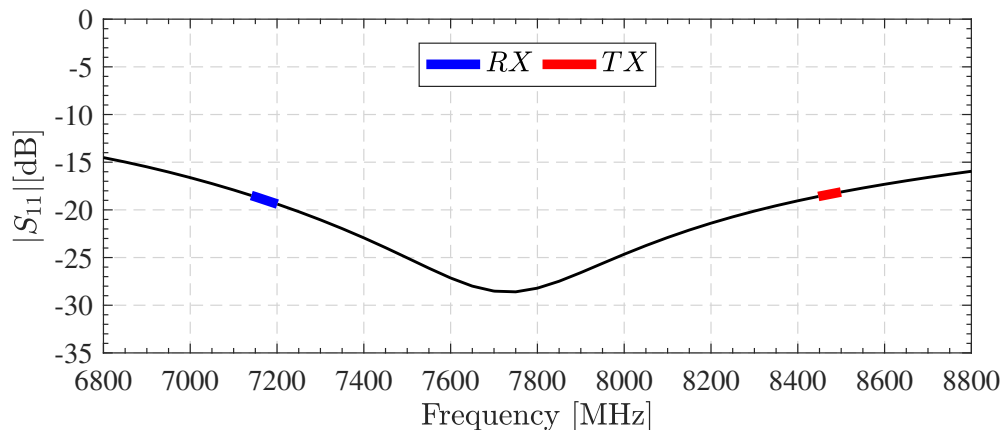


**Figure 6.8:** Simulated reflection coefficient for the vertically polarized TLGA. The return loss is greater than 18 dB for both the TX and RX band with a center frequency of 8475 and 7167.5 MHz respectively.

### 6.2.4 Summary and Specifications, V-pol TLGA

In Table 6.2 we summarize the simulated specifications of the TLGA in comparison to the requirements. The simulated directivity was greater than 1.3 dBi for both the RX and TX band in the desired coverage region. The gain requirement was at -1 dBi, thus there is a good margin for losses associated with e.g. a radome. Furthermore, the gain slope, in  $\theta$ , is well within the requirements with a simulated slope of about 0.2 dB per degree in the coverage region. The return loss exhibits good performance with a level that is greater than 18 dB for both bands. The side lobes are also suppressed to the required levels.

For a ground based application, e.g. telecommunication, the antenna can be used and manufactured as is. For use as a TLGA on a spacecraft a cylindrical radome of e.g. fiberglass should be attached around the antenna to provide the required mechanical stiffness. A coating, such as a blanket of Kapton, should furthermore be applied to protect against radiation charging. Thermal mismatches also need to be accounted for, refer to section 6.4.5 for a discussion on how this will be solved.

**Table 6.2:** Comparison table of the requirements versus the simulated values for the presented vertically polarized spline-optimized TLGA. Note that the simulated values are directivity.

| <i>Parameter</i>          | <i>Required (RX+TX)</i>          | <i>Simulated (RX+TX)</i>                 |
|---------------------------|----------------------------------|--|
| Gain                      | >-1 dBi @ $\theta=90\pm 20$ deg. | >1.3 dBi @ $\theta=90\pm 20$ deg.        |
| Gain slope (in $\theta$ ) | <1 dB / deg.                     | <0.2 dB / deg.                           |
| Return loss               | >16 dB                           | >18 dB                                   |
| Far-out side lobes        | <-10 dBi                         | $\sim -9.5$ dBi (TX) $\sim -13$ dBi (RX) |

### 6.3 Three Layer Meander-Line Polarizer

A three layer polarizer was designed using the theory outlined in section 3. A flame resistant fiber glass (FR4) substrate was selected for its mechanical robustness and low loss characteristics. In the first subsection we present how the layers can be modelled using a unit cell approach. The results for the ideal case, where a plane wave is incident on the polarizer, is presented in the second subsection. The final subsection will treat results of the meander pattern wrapping around cylinders.

#### 6.3.1 Plane Meander Array

The polarizer was modelled using a full wave unit cell approach as illustrated in Figure 6.9. Using symmetry planes, perfect E and H, the three meander layers are modelled as infinite with a incident plane wave. Due to the use of symmetry planes each component of the incident field i.e. the vertical and horizontal has to be studied separately, hence the two modelling configurations in Figure 6.9. Note that for optimization and tuning purposes, since we need to make use of two models, using HFSS alone will not work and an external software is required that can control both model parameters simultaneously. A similar software approach, as described in section 5.2, was employed but with different objectives.

The parameters of the final, plane, polarizer design is shown in Table 6.3. Refer to section 3 for parameter visualisation. The spacing between the layers was, after optimization, 9.18 mm using a FR4 substrate with relative permittivity of 4.4 and a thickness of 12 mil.

**Table 6.3:** Parameters for the three layer, plane, meander line polarizer using a FR4 substrate with a relative permittivity of 4.4 and thickness ( $t$ ) of about 12 mil. The parameters are illustrated in Figures 3.2 to 3.4. The layer spacing ( $s$ ) is 9.180 mm.

| <i>Param. [mm]</i> | <i>Layer 1</i> | <i>Layer 2</i> | <i>Layer 3</i> |
|--------------------|----------------|----------------|----------------|
| $p$                | 6.826          | 6.826          | 6.826          |
| $d$                | 0.2081         | 0.8323         | 0.2081         |
| $w$                | 5.065          | 5.065          | 5.065          |
| $a$                | 10.901         | 10.901         | 10.901         |

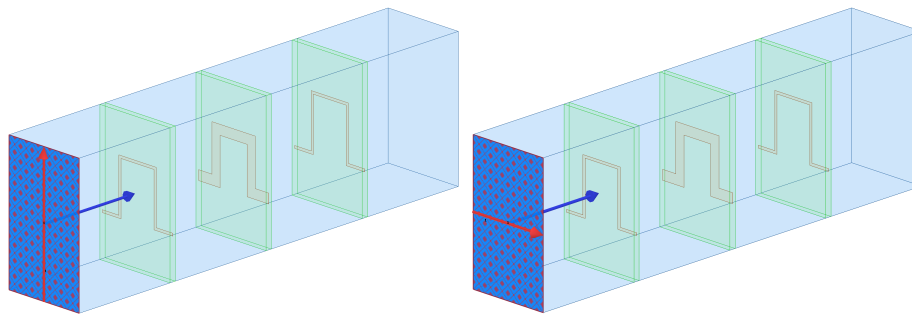


**Figure 6.9:** Illustration of the meander unit cell modelling, one for each polarisation component as defined by the red arrows. The blue arrow is an indication that the measured characteristics are de-embedded. Symmetry planes are employed in order to simulate an infinite array of meander cells with an incident plane wave.

**Table 6.4:** Parameters for the three layer, cylindrical, meander line polarizer using a FR4 substrate with a relative permittivity of 4.4 and thickness ( $t$ ) of about 12 mil. The parameters are illustrated in Figures 3.2 to 3.4. The layer spacing ( $s$ ) is 9.180 mm. The three layers are displayed in Figure 6.12 which are wrapped using the rhombic shaped plane in Figure 6.11.

| <i>Param. [mm]</i> | <i>Layer 1</i> | <i>Layer 2</i> | <i>Layer 3</i> |
|--------------------|----------------|----------------|----------------|
| $p$                | 6.920          | 6.952          | 6.970          |
| $d$                | 0.2081         | 0.8323         | 0.2081         |
| $w$                | 5.065          | 5.065          | 5.065          |
| $a$                | 10.697         | 10.661         | 10.640         |
| $R$                | 26.484         | 35.992         | 45.50          |
| $H$                | 37.0           | 53.0           | 85.0           |

### 6.3.2 Ideal AR, XPD and Return Loss

The axial ratios, cross-polar discriminations and reflection coefficients of the designed, plane, polarizer are displayed in Figure 6.10. The axial ratio and XPD display very good characteristics with a level that is better than 31 dB for the latter for both bands. The reflection coefficient, due to the modelling approach, has to be divided into parallel and perpendicular components of the incident field, refer to Figure 3.3. For the RX band the reflection is lower than -12.5 and -16.5 dB respectively for the perpendicular and parallel components. Similarly for the TX band where it is lower than -22 and -25 dB for the two components. One can argue why the reflections were not shifted to left, in order to obtain better levels at both bands, by tuning substrate spacings. The answer is simply that a trade-off has to be made between XPD and  $S_{11}$ , refer to the theory outlined in chapter 3. If a potential customer finds the return loss not satisfactory at the RX band a four layer approach can be used to improve the matching.

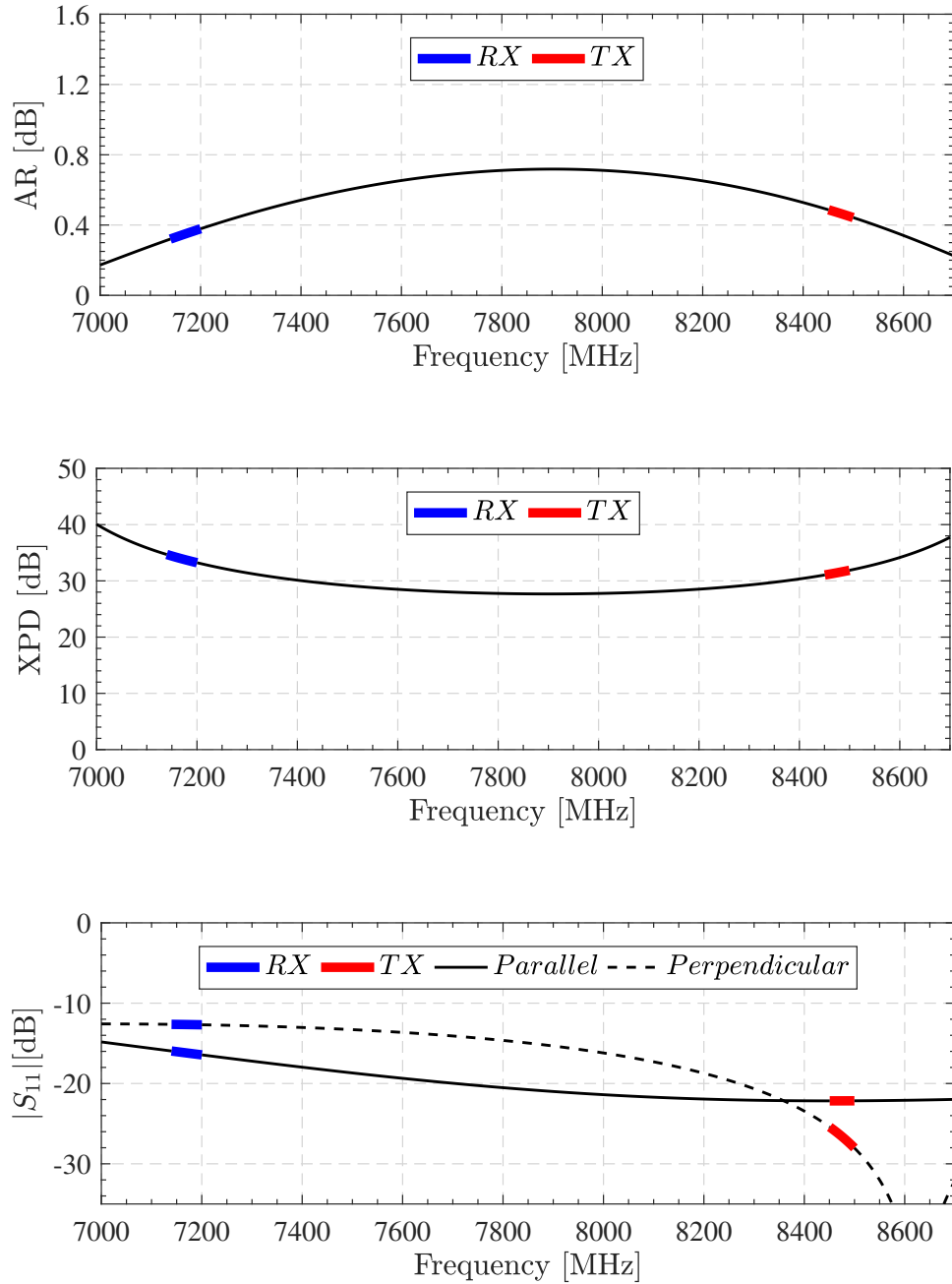


**Figure 6.10:** Axial ratio, cross-polar discrimination and reflection coefficients, perpendicular and parallel components, for the meander line polarizer. The results assume plane wave incidence on three layers of infinite extension.

### 6.3.3 Cylindrical Wrapping of Polarizer

The ideal case, as mentioned, is a plane wave incident on a polarizer of infinite extension as modelled and presented in section 6.3.1. However, cylindrical sheets of meander layers are required for the antenna at hand. Using the proposed conversion method, from a plane polarizer to a cylindrical, in section 3 we present the parameters of the three layer polarizer. All parameters are illustrated in Figure 3.2 to 3.4. The rhombic shaped meander plane, which was wrapped around the FR4 substrate, is shown in Figure 6.11. Note that the angle of the meander lines, i.e.  $\pm 45^\circ$ , determines whether the incident vertically polarized will be right or left handed circularly polarized respectively.

One important thing to note is that the periodicity of the first and last meander line on the cylinder need to be aligned in order to eliminate any discontinuities. We employed a method where the last meander line, refer to Figure 6.11, was moved to a position just left of the first meander line in the modelling software. The periodicity,  $p$  in Figure 3.2, was further tuned until alignment was achieved whereas the last meander line was moved back to its original position. The consequence is, of course, that the periodicity is slightly deviated from the optimal value as derived in the tuning and optimization process of the plane layers. The tuning was performed to micrometer level but one could, of course, argue that the number decimal points presented in Table 6.4 can be very hard to achieve in a manufacturing process. Slight deviations from simulations and actual manufactured design can thus be expected. The final geometry, for all three layers, are displayed in Figure 6.12 with corresponding radii and heights in Table 6.4.

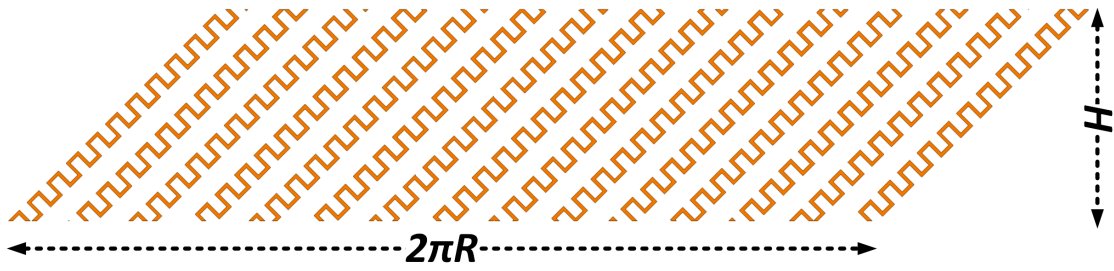


**Figure 6.11:** The figure display the rhombic shaped meander plane that is wrapped around a cylinder, in this case a FR4-epoxy substrate. The meander plane is the result from an intersection between a very large quadratic shaped polarizer plane and a rhombic parallelogram. The geometry of the parallelogram is matched to the dimensions of the cylinder with radius  $R$  and height  $H$ .

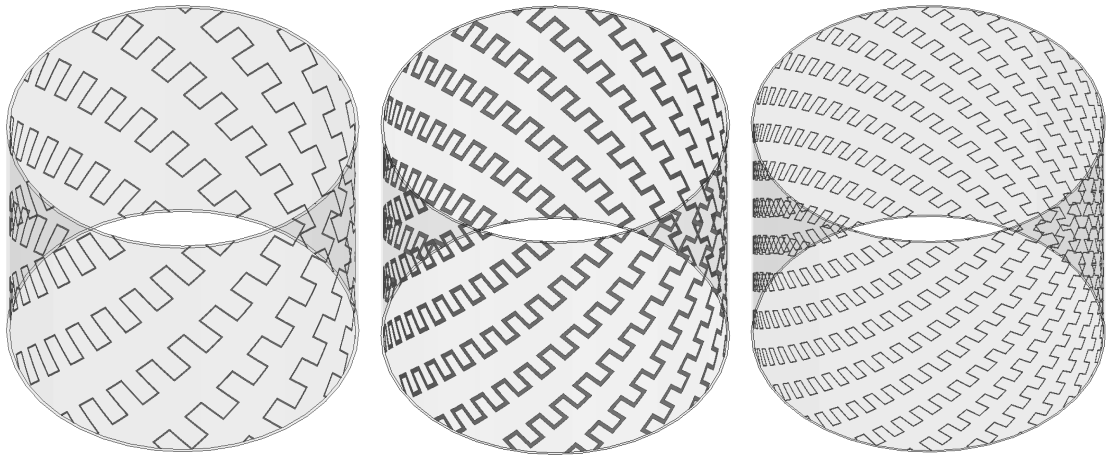


**Figure 6.12:** Illustration of the three layer polarizer used for the biconical antenna. The meander lines are wrapped on a cylindrical FR4 substrate with a thickness of 12 mil. The innermost layer is the left cylinder and the outermost to the right. Note that the illustrated polarizers are scaled versions of the actual design. Refer to Figure 6.13 to observe how the layers are implemented in the design.

## 6.4 Dual Band Circularly Polarized TLGA

The presented dual band RHCP TLGA is based on the vertically polarized variant in section 6.2. The addition is the designed meander line layers as presented in section 6.3 that also provides mechanical robustness. In the first subsection we show how the three layers are positioned on the antenna. The remaining subsections treat the simulated results such as radiation pattern, axial ratio, reflection coefficients and mechanical considerations.

### 6.4.1 Positioning of Polarizer Layers

The ideal case, as mentioned, would be a plane wave incident on the polarizer in order to make use of the full characteristics, with e.g. a XPD better than 31 dB, as shown in Figure 6.10. If we are very far from the antenna we can approximate the propagating wave front as plane, consequently we would like to position the polarizer layers as far away as possible. But always present are the mechanical considerations of the antenna and especially, for a space antenna, it must survive the launch of the spacecraft. The meander layers must be placed in a manner that stabilizes the structure. Furthermore, the layers must be very precisely aligned to decrease the degradation of the optimized performance of the meander spacing. A space antenna should also avoid, or minimize, the use of dielectrics to avoid charge build up. Consequently no dielectric can be used to align the layers and account for obliquely incident waves from the phase center.

The three meander layers were positioned as according to Figure 6.13 in the simulations. The figure is a cutting plane illustration of the antenna. The outer layer is positioned just outside the bicone and the two inner layers inside the profile. The spacing, height and radii of the different layers are outlined in section 6.3.3. Alignment and robustness, in all degrees of freedom, are achieved by making small ridges in the profile where the substrates can be glued to the aluminium cones. Thermal mismatches can be accounted for by having a coaxial feed that is capacitively coupled, refer to the illustration in Figure 6.13.

### 6.4.2 Elevation Beam Patterns

The elevation beam patterns of the circularly polarized TLGA are displayed in Figure 6.14 where the upper plot is the RX frequencies and the lower the TX. The co and cross-polarisation is shown in red and blue corresponding to RHCP and LHCP respectively. If we compare the results with the vertically polarized antenna in Figure 6.7, without the meander layers, we can observe that the beam shape is retained. However, the side lobes are slightly degraded for the RHCP antenna. Furthermore the pattern is not entirely symmetric around the beam peak, which as discussed in section 6.2.2, is due to the non ideal feed. However, the polarizer itself is not a rotational symmetric structure, and discontinuities exist especially at higher elevation angles of meander cylinders. Thus we should not expect a perfectly symmetric pattern even if the feed effect was not present.

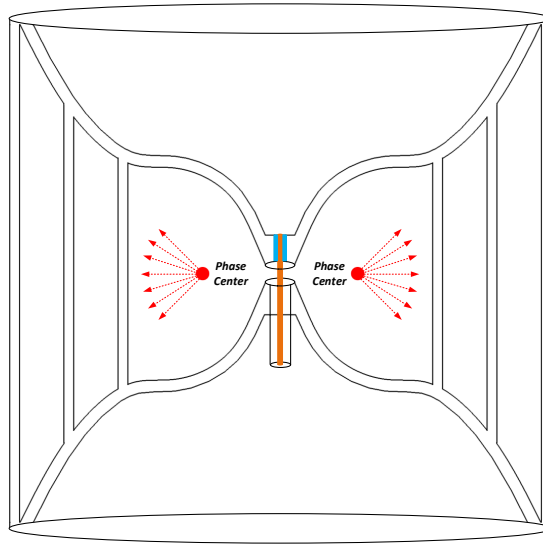


**Figure 6.13:** A cutting plane illustration of the circular polarized TLGA. The figure displays the relative positions of each polarizer layer. The spherical phase front, incident on the layers, is also illustrated. The blue area indicates the dielectric that should be used in the capacitive coupling of the coaxial feed.

### 6.4.3 Axial Ratio and XPD

Axial ratio and cross-polar discrimination are essentially scaled versions of each other as shown by e.g. equation 4.4. But depending on the specification sheet used, both can be useful to show. The AR and XPD of the antenna for RX band frequencies are displayed in the upper and lower plot of Figure 6.15 respectively. At the beam center a XPD of around 17.5 dB was obtained, note that the XPD significantly increases for angles around  $\theta = 90^\circ$ . Similarly for TX band frequencies in Figure 6.16 but the XPD was lower, at a level of about 11.5 dB at the beam center and increasing for higher and lower elevation angles around  $\theta = 90^\circ$ . If we go back and look at the optimized plane polarizer results in Figure 6.10 this result was expected since we have slightly degraded performance, in terms of XPD, for the TX band in comparison to the RX. A XPD level greater than 31 dB which was derived for the plane polarizer in Figure 6.10 was not achieved. Referring to previous discussions in e.g. section 6.3.3 and 3 this was expected due to several factors. Firstly, the meander planes that are optimized need to be converted to cylindrical which slightly changes e.g. the periodicity and distance between the lines. Secondly, and probably the most predominant factor, is that the first layers are close to the phase center of the horn. As such, the performance of the polarizer was degraded due to obliquely incident waves. Yet, the XPD performance was within the requirement of 10 dB. Uncertainties and small model errors can not be avoided so an actual manufactured antenna will exhibit slightly different characteristics. If it will be in a positive or negative direction, performance wise, cannot be said at this stage but we have a good margin for the requirements.

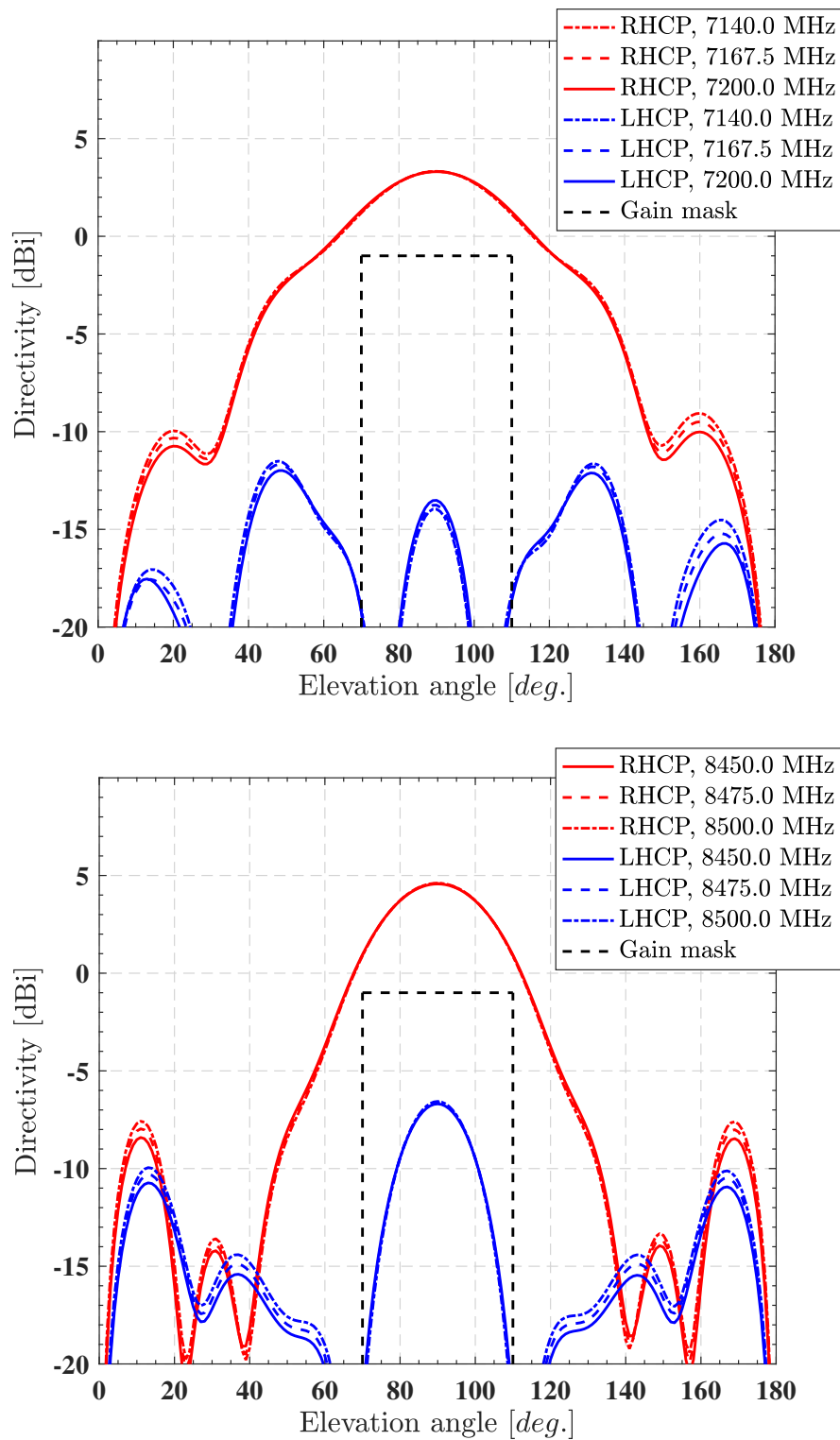


**Figure 6.14:** Beam patterns, with co and cross-polarisation in red and blue respectively, for the two bands i.e. RX band upper plot and TX lower plot. The gain mask is indicated in dotted black.

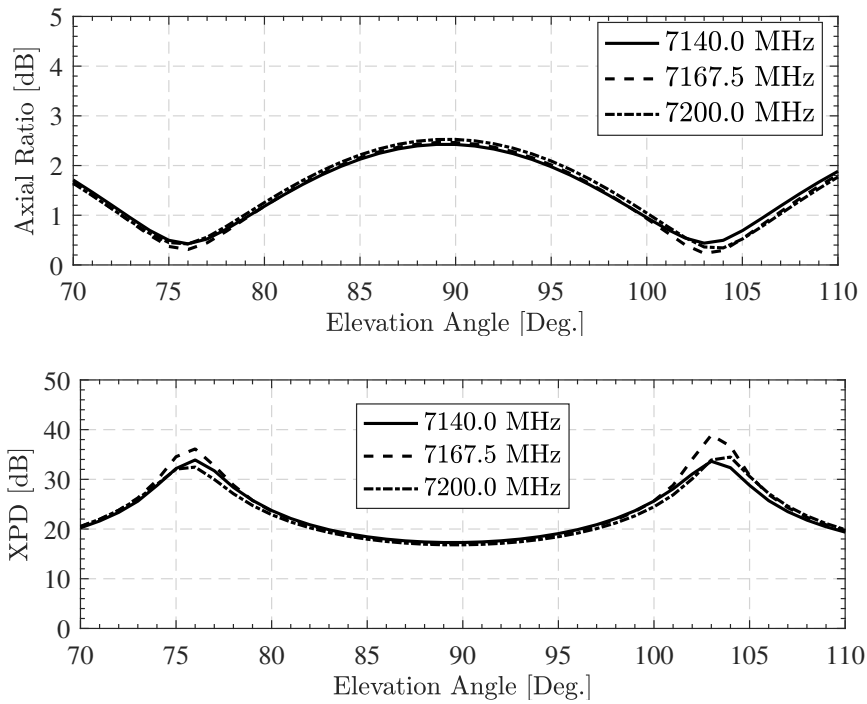


**Figure 6.15:** Axial ratio, upper plot, and cross-polar discrimination, lower plot, for RX band frequencies of the proposed RHCP TLGA. The presented results are averaged for all phi cuts to better illustrate different behaviours across the band.

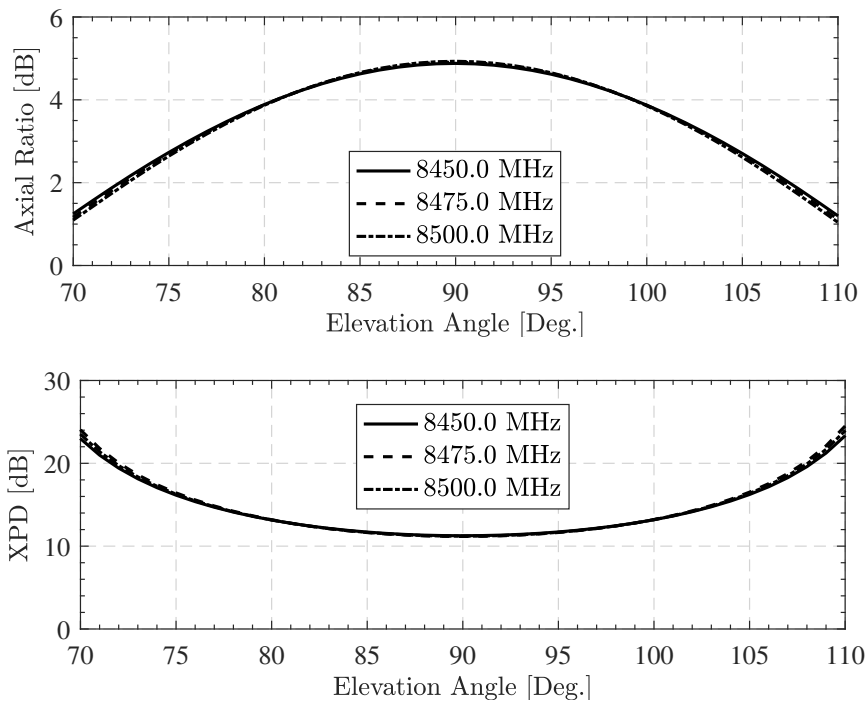


**Figure 6.16:** Axial ratio, upper plot, and cross-polar discrimination, lower plot, for TX band frequencies of the proposed RHCP TLGA. The presented results are averaged for all phi cuts to better illustrate different behaviours across the band.

### 6.4.4 Reflection Coefficients

The simulation of the full structure, including all meander layers, was extremely heavy in terms of CPU and RAM usage. After a significant effort on optimizing the mesh of the antenna geometry we managed to simulate the structure using a eight core Xeon with 64 GB of RAM. For the RHCP TLGA we thus only present a few frequency points for the reflection coefficient as displayed in Figure 6.17. The simulation time for the 11 presented points were about six days which also includes the radiation pattern analysis. In this sense, we also see why e.g. the geometry of the meander cells were not re-optimized due to difference associated with the plane to cylinder conversion. The benefits of the latter would probably, however, only correlate to moderate performance improvements.

The reflection coefficients for the antenna are displayed in Figure 6.17. The three points, i.e. the lower, center and upper frequencies for the RX band is displayed in blue and similarly for the TX band in red. The five black dots are simulated values outside the used bands. The reflection coefficients are below -14 and -18 dB respectively for the RX and TX bands.

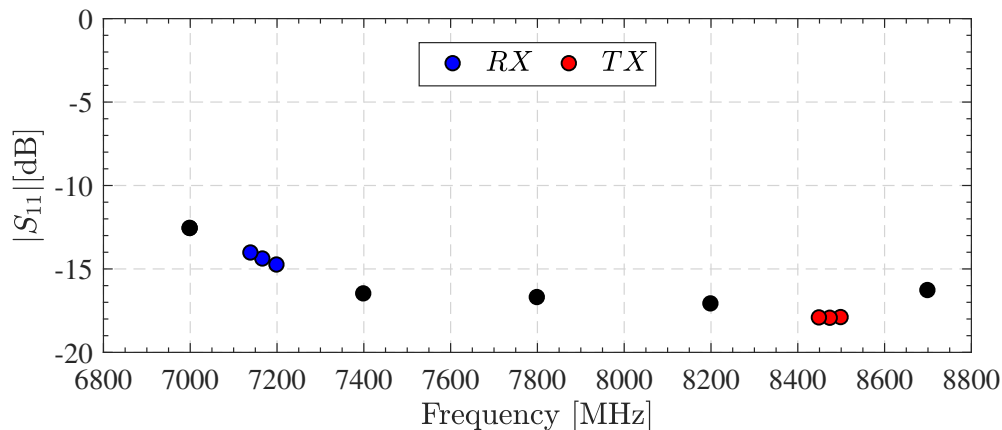


**Figure 6.17:** Simulated reflection coefficient for the circularly polarized TLGA. The blue and red dots indicate the TX and RX band frequencies respectively. The black dots are simulated values outside the used bands.

### 6.4.5 Summary and Specifications, RHCP TLGA

The simulated results of the RHCP TLGA are displayed in column three of Table 6.5 together with the requirements in column two. At the edge of the coverage region the directivity was greater than 0.9 dB for the TX band and slightly higher for the RX band. This leaves a good margin for the gain requirement of -1 dBi. The return loss is 2 dB below the requirement for the lower frequency in the RX band. Since we have introduced a polarizer, and thus changing the wave behaviour as well as reflections, the bicone can benefit from a re-optimization of the gap size (G in Figure 2.1). Considering the mesh heavy antenna, the simulations take a very long time as discussed in section 6.4.4. The best solution is to manufacture a prototype, where it will be possible to tune the gap size by hand and observe the changes on a vector network analyser. However, 14 and 18 dB return losses are still good values and can probably be accepted for usage even on state-of-the-art satellites and spacecrafts. Continuing with the specifications in Table 6.5 a moderate degradation of the sidelobe levels was seen and the dominant sidelobes are at a level of approximately -10 and -8 dBi respectively for the two bands. The XPD was at a level of about 11.5 dB at the TX band and 17.5 dB at the RX band which leaves a good margin for the requirement of 10 dB. A 3D model, as electrically simulated, of the antenna is displayed in Figure 6.18. The upper figure is the full antenna as seen from the side whereas the lower figure is a, slightly tilted, cutting plane illustration.

**Table 6.5:** Comparison table of the requirements versus the simulated values for the RHCP spline-optimized TLGA. Note that the simulated values are directivity.

| <i>Parameter</i>          | <i>Required (RX+TX)</i>          | <i>Simulated (RX+TX)</i>           |
|---------------------------|----------------------------------|------------------------------------|
| Gain                      | >-1 dBi @ $\theta=90\pm 20$ deg. | >0.9 dBi @ $\theta=90\pm 20$ deg.  |
| Gain slope (in $\theta$ ) | <1 dB / deg.                     | <0.2 dB / deg.                     |
| Return loss               | 16 dB                            | >14 dB (RX)   >18 dB (TX)          |
| Side lobe levels          | <-7 dBi @ far edge angles.       | <-10 dBi (RX)   $\sim$ -8 dBi (TX) |
| Polarisation              | RHCP                             | RHCP                               |
| XPD                       | 10 dB                            | >17.5 dB (RX)   >11.5 dB (TX)      |

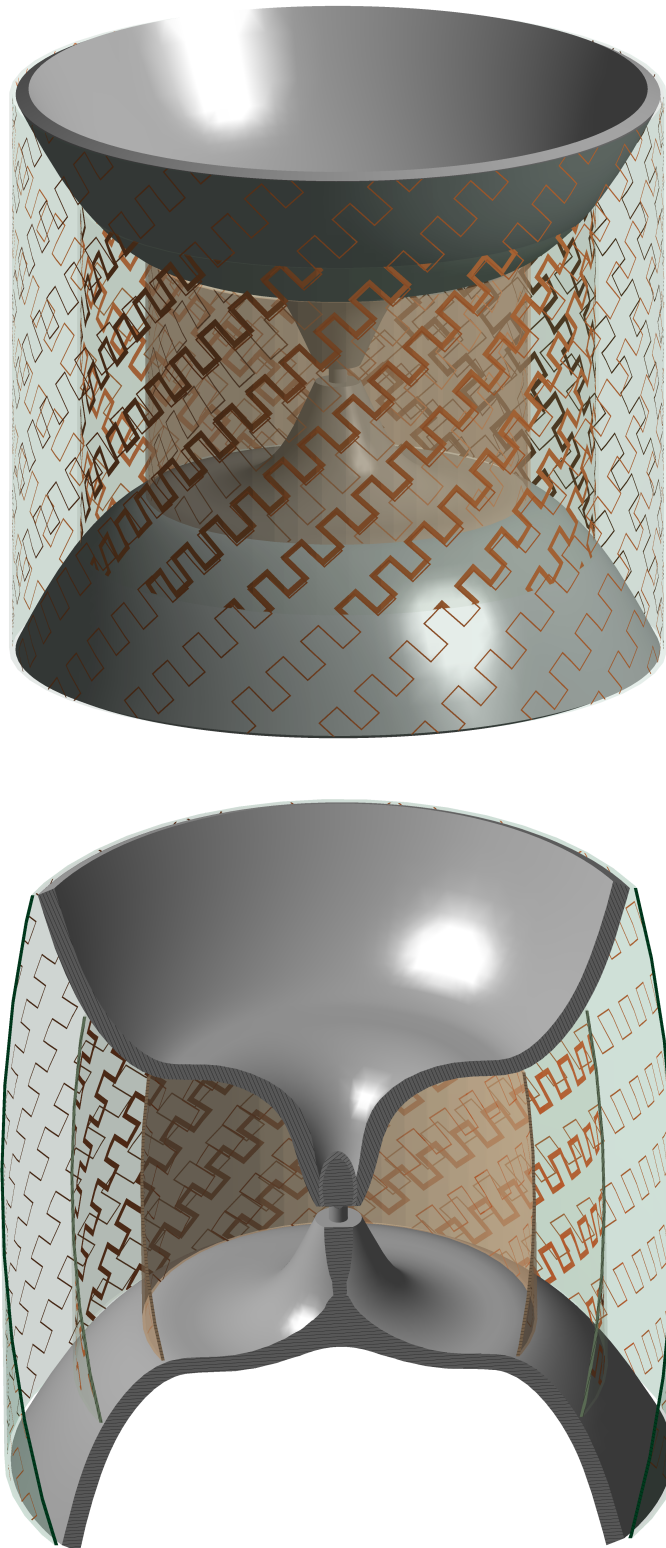


**Figure 6.18:** Electrical model of the final circularly polarized dual band antenna. The upper figure is the full 3D model whereas the lower plot is a, slightly tilted, cutting plane.

## 6.5 RHCP TLGA as Single Band Antenna

The design frequency for the two proposed antennas is at the center of the two bands i.e. the geometric mean of 7.14 and 8.5 GHz. How the antenna performs at the design frequency is of great interest for cases where the antenna should function as either a TX or RX antenna. The design could be very useful for example in telecommunications or very wide-band satellite telemetry. A stacked element configuration, one RX and one TX antenna, could be required for the latter. Recall that all presented designs are scaleable in frequency to other bands such as  $K_u$ . Note that the section also provides information for the dual band designs as a verification that nothing unexpected, such as strange resonance behaviours, happens in between the bands.

The radiation pattern, in steps of 0.1 GHz, from 7.3 to 8.3 GHz is shown in the lower plot of Figure 6.20. We also display the radiation pattern, in a more narrow band, around the design frequency ( $\approx 7.79GHz$ ) in the upper plot of Figure 6.20 for a clear view of some of the best characteristics. I.e. side-lobe suppression lower than -15 dBi, approximately constant directivity and good margins for the gain mask across the band. The cross-polarisation (LHCP) is not shown, instead we display the XPD in Figure 6.19 for the frequency range 7.3 to 8.3 GHz in steps of 0.1 GHz. For the narrowband range in the upper plot of Figure 6.20 the XPD is observed to be better than 16 dB. The reflection coefficient of the antenna is, of course, the same as shown in Figure 6.17 and is lower than -16 dBi. Note that the data is averaged for all phi cuts. A small omni-variation is present due to non-symmetries in the polarizer.

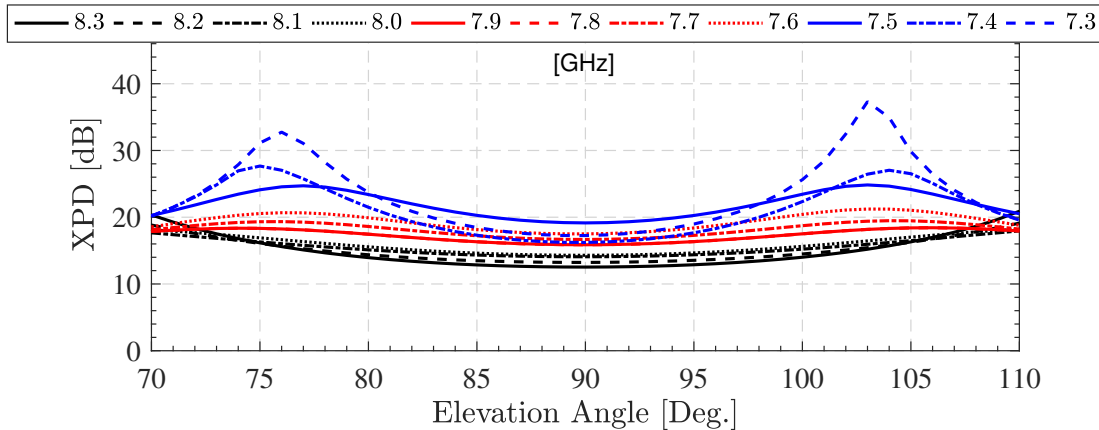


**Figure 6.19:** The cross-polar discrimination is shown for a large band, from 7.3 to 8.3 GHz, for the RCHP TLGA. The displayed plots are averaged for all phi cuts, a small omni-variation can be expected due to non-symmetries in polarizer.

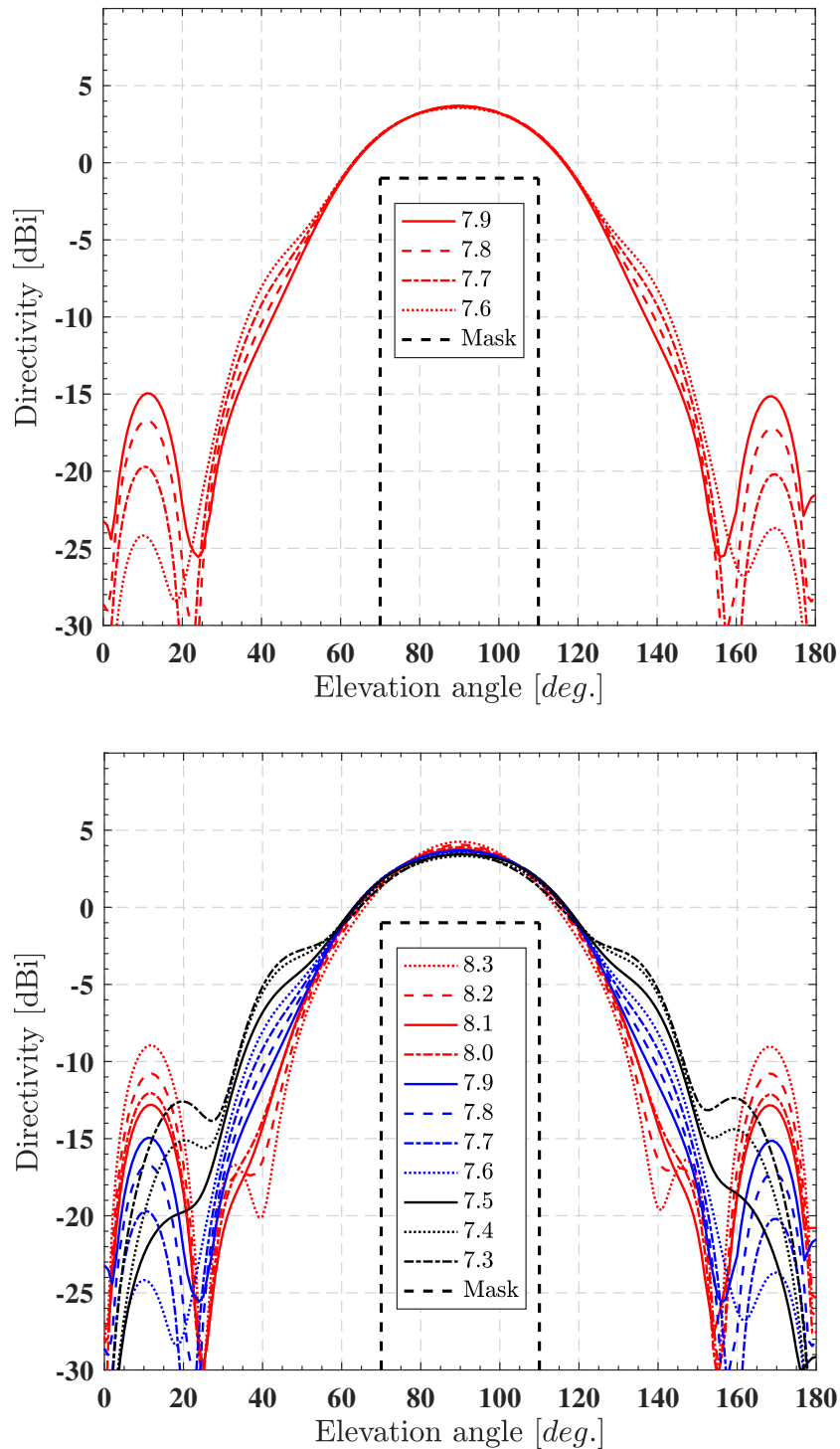


**Figure 6.20:** The lower plot displays the beam pattern of the co-polarization, i.e. RHCP, of the biconical horn for the frequency range 7.3 to 8.3 GHz. The top plot displays the same information as the lower plot but in a more narrow band around the center frequency. The plots can be used as reference for how well the antenna would be able to perform in single band operation.



# 7

## Discussion and Conclusions

A circularly polarized spline-defined, stochastically optimized, dual band biconical horn has been presented. A set of new profiles for the bicone were investigated, previously this has only been done in a very limited sense. From the profile investigation we can conclude that a lot can be gained in terms of both directivity, side-lobe levels and size of the antenna. E.g. using a sinusoidal profile the size of antenna can be reduced by a factor greater than two while still maintaining the same directivity. The sinusoidal profile also provided a good foundation for a dual band design. The gain margins and side-lobe levels were, however, insufficient for the requirements at hand. Corrugations could be one way to solve some of the issues, but a corrugated antenna is a mechanically complex antenna and requires very precise and specialised equipment and thus renders an expensive antenna. We employed a more elegant and modern approach where the profile was defined by a set of interpolated points that were optimized using biologically inspired optimization methods. The approach proved to be very effective for shaping the radiation pattern and requirements were met.

Through the design of a three layer cylindrical polarizer the field was converted to circular, an important requirement for many space systems. Furthermore a robust flame resistant fibreglass substrate was used in the design to provide the mechanical stiffness required for a spacecraft launch. Thermal mismatches can be accounted for by using capacitive coupling at the excitation gap. The capacitive coupling allows the center conductor of the feed to float in relation to the upper cone of the bicone. A significant improvement, and a new development, in the presented design is that it only requires one bicone element for both RX and TX whereas designs by e.g. RUAG Space and RYMSA require two elements. This drastically changes the mechanical and electrical complexity as well as the cost, size and weight of the antenna.

### 7.1 Future work

The complete design cycle of a space antenna, from electrical, mechanical, thermal design to farfield measurements in an anechoic chamber, vacuum cycling, vibrational tests, outgassing and thermal tests requires a team of experienced engineers. In this sense, the thesis was intentionally limited and much work is left to be done for the antenna to actually fly in space. Yet, this thesis shows how space TLGAs can be simplified, in many ways, and still perform equal or better than current designs.

Thus for the presented design a manufactured prototype may be close if a mechanical engineer can be dedicated to the project.

In the first subsection we will discuss some of the electrical characteristics and how they could be improved if e.g. a future space system would require better performance. The final subsection treats the future work in terms of mechanical and thermal design.

### 7.1.1 XPD and Return Loss Improvements

The axial ratio, which is directly associated with the cross-polar discrimination according to equation 4.4, can be significantly improved if desired. Firstly, if we e.g. design the antenna for higher gain the radius and aperture height is increased and the layers will be positioned further away from the phase center, assuming that the phase center movement is small in the radial direction. This will significantly improve the polarizer performance. Secondly, we may also position the layers differently in the current design by having two layers attached to the profile and one further outside using, for example, honeycomb spacers. The latter may, however, not be optimal for usage in space.

The return loss was found to be greater than 14 and 18 dB respectively for the RHCP TLGA. Due to the heavy simulations the values were not optimized further. The best solution to improve the reflections are to manufacture a prototype and measure the changes using a vector network analyzer through tuning e.g. the gap size. Another approach to improve the return loss is to use a four layer polarizer. Also recall that the feeding coaxial line is  $50 \Omega$  with no matching stage. Thus another possibility for improving the return loss is, of course, to use a matching stage. The latter can e.g. be combined with a wave guide to coaxial transition, if wave guide feeding would be required by, for example, an upcoming satellite system.

In this thesis, the retrieved values of AR, XPD and return loss were found sufficient and proves the workings of the technology and that it can qualify for the electrical requirements of a space TLGA.

### 7.1.2 Mechanical and Thermal Design

Mechanical and thermal design engineers should be dedicated to the final design of the antenna. The engineers should focus on the following subjects

- Mounting plate and SMA-connector. A standard sized coaxial feed may not work due the small radii of the inner conductor. Thus, a dedicated  $50 \Omega$  design may be needed to survive the launch of a spacecraft. This can be quickly determined through Ansys Workbench simulations with the designed meander layers.

- Consider ways to mount the meander layers. We propose using ridges in the profile where the two inner layers can be glued whereas the outer layer is attached outside of the cones. Refer to Figure 6.13.
- The meander-lines need to be grounded to the bottom cone to avoid static discharges. This can be solved by employing e.g. ground rings.
- Multipaction analysis to determine breakdown voltages and power handling.
- Thermo-elastic calculations need to be performed using for example advanced simulation softwares such as Ansys Workbench. Hand calculations for the thermal mismatch between the coaxial connector and the upper cone may be a good initial approach in order to have a foundation for the continued design.
- Charge protection radome and material considerations. A layer of Kapton on the outer meander layer is a straight forward solution for the former.



# Bibliography

- [1] S.W. Hawking, *A Brief History of Time: from the Big Bang to Black Holes*, Bantam, 2011, ISBN 978-0-857-51004
- [2] D.K Cheng, *Field and Wave Electromagnetics*, Person, 2014, ISBN 978-1-292-026565
- [3] J.C Maxwell, *A Dynamical Theory of the Electromagnetic Field*, Phil. Trans. R. Soc. Lond, Jan. 1865, pp. 459-512
- [4] W.A. Imbriale et al, *Space Antenna Handbook*. Vol. 1, John Wiley & Sons , 2012, ISBN 978-1-119-993193
- [5] S. Lotfollah et al, *Handbook of Reflector Antennas and Feed Systems Volume II: Feed Systems*. Vol. 2, Artech House, 2013.
- [6] J. Mitola, "The Software Radio Architecture", IEEE Commun. Mag., vol 33, no 5, pp. 26-38, May 1995.
- [7] P. Cruz et al, "Designing and Testing Software-defined Radio", IEEE Microwave Mag., vol 11, no 4, pp. 83-94, June 2010.
- [8] Kepler Communications. *Kepler Satellites*. (2018, Jun., 10) [Online]. Available: <http://www.keplercommunications.com/>.
- [9] Dicke-switched Microwave Radiometry Using Ettus USRP and GNU Radio. (2018, May., 8) [Online]. Available: <http://gnuradio-ffts.readthedocs.io/en/latest/index.html>
- [10] J. D. Vacchione, R. C. Kruid, A. Prata, L. R. Amaro and A. P. Mittskus, "Telecommunications antennas for the Juno Mission to Jupiter," 2012 IEEE Aerospace Conference, Big Sky, MT, 2012, pp. 1-16.
- [11] J. Volakis. *Antenna Engineering Handbook*. Fourth Edition. McGraw-Hill Publishing, 2007, ISBN 978-0-071-47574-7
- [12] J. Zackrisson, "RUAG space activities in the TTC, GNSS and data-downlink antenna field," 2017 11th European Conference on Antennas and Propagation

- (EuCAP), Paris, 2017, pp. 529-533.
- [13] P. Ingvarson and J. Zackrisson, "Swedish space antenna projects," 2013 7th European Conference on Antennas and Propagation (EuCAP), Gothenburg, 2013, pp. 3161-3165.
- [14] J.Bäck, J.Zackrisson, "Circularly polarized slot antenna with toroidal coverage", European Conference on Antennas and Propagation (EuCAP), 2007, ESA SP-626.
- [15] F. Mayol, M. Padilla and J. M. Montero, "Turnstile-Junction-Based Omnidirectional Antennas for Space Applications", IEEE Antennas and Propagation Magazine, vol. 53, no. 3, pp. 255-262, June 2011.
- [16] P-S. Kildal. *Foundation of Antennas: A Unified Approach for Line-Of-Sight And Multipath*. 2015 Edition. Sweden: Kildal Antenn AB, 2015, ISBN 978-1-608-07867-7.
- [17] T. A. Milligan. *Modern Antenna Design*. 2nd Edition. NJ, USA: Wiley-IEEE Press, 2005, ISBN 978-0-471-45776-3.
- [18] C. A. Balanis. *Antenna Theory: Analysis and Design*. 4th Edition. NJ, USA: Wiley, 2016, ISBN 978-1-118-64206-1.
- [19] C. A. Balanis. *Modern Antenna Handbook*. 1st Edition. NJ, USA: Wiley, 2008, ISBN 978-1-118-64206-1.
- [20] C. H. Papas and R. King, "*Radiation from Wide-Angle Conical Antennas Fed by a Coaxial Line*", Proc. I.R.E., vol. 39, no. 1, pp. 49-51, Jan. 1951.
- [21] C. H. Papas and R. King, "*Input Impedance of Wide-angle Conical Antennas Fed by a Coaxial Line*", Proc. I.R.E., vol. 37, pp. 1269-1271, Nov. 1949.
- [22] W. L. Barrow et al., "*Biconical Electromagnetic Horns*", in Proceedings of the IRE, vol. 27, no. 12, pp. 769-779, Dec. 1939.
- [23] C. Granet, "*Profile options for feed horn design*", 2000 Asia-Pacific Microwave Conference. Proceedings (Cat. No.00TH8522), Sydney, NSW, 2000, pp. 1448-1451.
- [24] A. Akgiray, "New Technologies Driving Decade-Bandwidth Radio Astronomy: Quad-Ridged Flared Horn & Compound-Semiconductor LNAs", Ph.D. dissertation, California Institute of Technology, Pasadena, California, 2013. [Online]. Available: <https://thesis.library.caltech.edu/7644/>, Accessed on: May 13, 2018.

- 
- [25] A. Akgiray, S. Weinreb, W. A. Imbriale and C. Beaudoin, "Circular Quadruple-Ridged Flared Horn Achieving Near-Constant Beamwidth Over Multioctave Bandwidth: Design and Measurements," in *IEEE Transactions on Antennas and Propagation*, vol. 61, no. 3, pp. 1099-1108, March 2013.
- [26] C. A. Hacking, D. J. Hall, D. E. Wolf, "*Man/machine design of a broadband microwave circular polarizer*", 2nd Hawaii Int. Conf. System Sciences, 1969-Jan.-22-24.
- [27] L. Young, L. Robinson and C. Hacking, "*Meander-line polarizer*", in *IEEE Transactions on Antennas and Propagation*, vol. 21, no. 3, pp. 376-378, May 1973.
- [28] M. A. Joyal, M. Riel, Y. Demers and J. J. Laurin, "A Meander-Line Circular Polarizer Optimized for Oblique Incidence," in *IEEE Transactions on Antennas and Propagation*, vol. 63, no. 12, pp. 5391-5398, Dec. 2015.
- [29] Munk, Ben A. et al. *Finite Antenna Arrays and Fss*. John Wiley Sons, Incorporated, 2007, ISBN 978-1-280-55651-7.
- [30] R. Vincenti Gatti and R. Rossi, "*A Novel Meander-Line Polarizer Modeling Procedure and Broadband Equivalent Circuit*", in *IEEE Transactions on Antennas and Propagation*, vol. 65, no. 11, pp. 6179-6184, Nov. 2017.
- [31] C. Terret, J. Levrel and K. Mahdjoubi, "Susceptance computation of a meander-line polarizer layer," in *IEEE Transactions on Antennas and Propagation*, vol. 32, no. 9, pp. 1007-1011, Sep 1984.
- [32] Ruey-Shi Chu and Kuan-Min Lee, "Analytical method of a multilayered meander-line polarizer plate with normal and oblique plane-wave incidence," in *IEEE Transactions on Antennas and Propagation*, vol. 35, no. 6, pp. 652-661, June 1987.
- [33] Outgassing Data for Selecting Spacecraft Materials. (2018, Jun., 8) [Online]. Available: <https://outgassing.nasa.gov/>
- [34] European Space Agency Multipactor Calculator. (2018, May., 8) [Online]. Available: <http://multipactor.esa.int/>.
- [35] Ansys Inc. HFSS. (2018, May., 8) [Online]. Available: <http://www.ansys.com/products/electronics/ansys-hfss>.
- [36] MathWorks Inc. MATLAB. (2018, May., 8) [Online]. Available: <http://www.mathworks.com/products/matlab>.

- [37] M. Wahde, *Biologically Inspired Optimization Methods: An Introduction*. UK:WIT Press, 2008, ISBN 978-1-84564-148-1.
- [38] J. Kennedy and R. Eberhart, "Particle Swarm Optimization" in Proceedings of IEEE International Conference on Neural Networks, Perth, Australia, 27 Nov.- 1 Dec., 1995, vol. 4, pp. 1942 - 1948.
- [39] C. Granet and T. S. Bird, "*Optimization of corrugated horn radiation patterns via a spline-profile*", 2002 9th International Symposium on Antenna Technology and Applied Electromagnetics, St. Hubert, QC, Canada, 2002, pp. 1-4.
- [40] J. Yang, J. Flygare, M. Pantaleev and B. Billade, "Development of quadruple-ridge flared horn with spline-defined profile for band B of the Wide Band Single Pixel Feed (WBSPF) advanced instrumentation programme for SKA," 2016 IEEE International Symposium on Antennas and Propagation (APSURSI), Fajardo, 2016, pp. 1345-1346.